Energy & Environmental Science

PAPER

View Article Online
View Journal | View Issue

Check for updates

Cite this: *Energy Environ. Sci.*, 2023, **16**, 241

Pre-zeolite framework super-MIEC anodes for high-rate lithium-ion batteries†

Shitong Wang,‡[a] Lijiang Zhao,‡[b] Yanhao Dong,*[ac] He Zhu,[d] Yang Yang,[ef] Haowei Xu,[a] Baoming Wang,[g] Yakun Yuan,[hi] Yang Ren,[d] Xiaojing Huang,[j] Wei Quan,[kl] Yutong Li,[c] Yimeng Huang,[g] Charles M. Settens,[m] Qi He,[a] Yongwen Sun,[e] Hua Wang,[a] Zunqiu Xiao,[c] Wenjun Liu,[n] Xianghui Xiao,[j] Riqiang Fu,[o] Qiang Li,[p] Yong S. Chu,[j] Zhongtai Zhang,[c] Qi Liu,[d] Andrew M. Minor,[fq] Junying Zhang,*[b] Zilong Tang*[c] and Ju Li*[ag]

Zeolites, Prussian blue analogues (PBAs), and metal–organic frameworks (MOFs) rely on surface-like internal pore diffusions, which have generically low activation barriers to enable the rapid uptake of chemical species. Here we show that Wadsley–Roth oxides (WROs) with pore diameters of 2.5 Å $< d <$ 2.8 Å, while excluding molecules, enable very rapid diffusion of Li^+ in single-crystal particles >10 μm size. This supports full charge cycles at high rates of ~30C, which would rival the filling up of gasoline vehicles, while reducing the contact and side reactions with the electrolyte and enhancing the cycle life up to 10 000 cycles. Pore diffusion in WRO mixed ionic and electronic conductors (MIECs) differs from that in lithium intercalation compounds in the off-centered Li storage and low-coordination saddle points for migration. The reduced topological constraints per atom and large free volume in the host also lead to abnormally low or even negative thermal expansion and soft phonons, similar to other open frameworks such as zeolites, PBAs, and MOFs. Based on these guidelines, we have synthesized new composition ($Nb_9W_4Ti_4O_{42.5}$) and crystal size-coarsened H-Nb_2O_5 (>20 μm single crystals) with unprecedented performance.

Received 8th September 2022,
Accepted 23rd November 2022

DOI: 10.1039/d2ee02918a

rsc.li/ees

---

[a] *Department of Nuclear Science and Engineering, Massachusetts Institute of Technology, Cambridge, MA 02139, USA. E-mail: dongyh@mit.edu, liju@mit.edu*
[b] *School of Physics, Beihang University, Beijing 100191, China. E-mail: zjy@buaa.edu.cn*
[c] *State Key Lab of New Ceramics and Fine Processing, School of Materials Science and Engineering, Tsinghua University, Beijing 100084, China. E-mail: tzl@tsinghua.edu.cn*
[d] *Department of Physics, City University of Hong Kong, Kowloon, Hong Kong, 999077, China*
[e] *Department of Engineering Science and Mechanics and Materials Research Institute, The Pennsylvania State University, University Park, PA 16802, USA*
[f] *National Center for Electron Microscopy, Molecular Foundry, Lawrence Berkeley National Laboratory, Berkeley, CA 94702, USA*
[g] *Department of Materials Science and Engineering, Massachusetts Institute of Technology, Cambridge, MA 02139, USA*
[h] *School of Mechanical Engineering, Shanghai Jiao Tong University, Shanghai 200240, China*
[i] *Zhangjiang Institute for Advanced Study, Shanghai Jiao Tong University, Shanghai 201203, China*
[j] *National Synchrotron Light Source II, Brookhaven National Laboratory, Upton, NY 11973, USA*
[k] *China Automotive Battery Research Institute Co., Ltd., Beijing 101407, China*
[l] *General Research Institute for Nonferrous Metals, Beijing 100088, China*
[m] *Materials Research Laboratory, Massachusetts Institute of Technology, Cambridge, MA 02139, USA*
[n] *Advanced Photon Source, Argonne National Laboratory, Argonne, IL 60439, USA*
[o] *National High Magnetic Field Laboratory, Florida State University, Tallahassee, FL 32310, USA*
[p] *Beijing Advanced Innovation Center for Materials Genome Engineering, Institute of Solid State Chemistry, University of Science and Technology Beijing, Beijing 100083, China*
[q] *Department of Materials Science and Engineering, University of California, Berkeley, CA 94702, USA*

† Electronic supplementary information (ESI) available: Experimental and computational details, supplementary figures, supplementary tables, and supplementary references. See DOI: **https://doi.org/10.1039/d2ee02918a**

‡ These authors contributed equally to this work.

Broader context

The key components in lithium-ion batteries are battery electrodes, which must be superfast mixed ionic and electronic conductors (super-MIECs) with an effective activation energy of less than 250 meV. Across different material classes, diffusion energy barriers less than 250 meV are rare for lattice diffusion, yet frequently encountered in surface diffusion that usually requires a host framework with a pore diameter $d > 2$ Å. Well-known frameworks such as zeolites with internal pore diameters ranging from ~ 3 Å to 10 Å and other nanoporous materials can take up large quantities of H_2O (molecular diameter 2.8 Å), H_2, and CO_2 molecules. However, these large-pore open frameworks will not store too many alkali metal atoms due to their excessively large pore sizes, and are thus not suitable for energy-dense fast-charging lithium-ion batteries. Here we define ''pre-zeolite'' frameworks to mean crystals with percolating open pores with a diameter smaller than the size of H_2O, and therefore excluding water adsorption and molecular adsorption in general, while allowing surface-diffusion like superfast transport of Li^+. This work offers unique physical insights and a robust approach to developing super-MIEC anodes for high-rate batteries. It also bridges two general material families—nanoporous framework materials and conductive oxides.

Introduction

Mixed ionic and electronic conductors (MIECs) are widely used in solid oxide fuel/electrolysis cells, batteries, electrochromic devices, neuromorphic computing, *etc.*[1–5] Lithium-ion battery (LIB)'s cathode and anode must be MIECs, and need to store large quantities of Li^0 on-demand in the lattice interior, accompanied by the redox of certain host elements, often transition metals (TMs). Rapid Li^+ and e^- transport (thus effective Li^0 ''atomic'' diffusivity D_{Li}) should be maintained at all depths of discharge (DODs), which is the most crucial factor for fast charging and high discharge power batteries used in heavy transportation (*e.g.*, boats, trains, and trucks), industrial equipment (*e.g.*, cranes), household products, and electrical-grid regulation.[5–15] Drawing an analogy to superionic solid electrolytes, we define super-MIECs in the LIB context to mean having an effective activation energy Q of D_{Li} inside the MIEC of less than 250 meV or about 10 k_BT at T = 300 K, which would give $D_{Li} \sim \nu_{Li}h_{Li}{}^2e^{-10} \sim 5 \times 10^{-13}$ m^2 s^{-1}, for a typical hopping trial frequency ν_{Li} = 1 THz and a hopping distance h_{Li} = 1 Å. This means in t = 100 seconds (the typical duration it takes to fill up a gasoline car), or in a full charge/discharge cycle at 36C, the diffusion distance $L = (2D_{Li}t)^{1/2}$ = 10 μm, which is the desirable battery electrode particle size for slurry coating. Note that a super-MIEC with a large DOD range would allow fully dense, single-crystal particles of 10 μm size to be used without requiring electrolyte infiltration into polycrystalline secondary particles, greatly increasing the volumetric energy density and reducing the side reactions. This is superior to nano $Li_4Ti_5O_{12}$ (the most widely studied and commercialized anode for fast charging[16]) with low D_{Li}. Some reported oxide anodes can be viewed as super-MIECs[12,17–19] (especially for Nb-based materials with >1 μm size, Table S1, ESI†), which can support a full charge/discharge cycle within several minutes.

The dual demands of large ''Li adsorption'' per volume and maintaining $D_{Li} \geq 5 \times 10^{-13}$ m^2 s^{-1} put stringent requirements on transition-metal oxide MIECs. Across material classes, diffusion barriers generically less than 250 meV are frequently encountered only in surface diffusion. Diffusion in tight-fitting atomic channels for the Li^+ cation (Shannon ionic diameters of 1.18 Å for 4-fold coordinated, 1.52 Å for 6-fold coordinated and 1.84 Å for 8-fold coordinated Li^+), such as inside $LiFePO_4$, typically gives Q values ranging from 270 meV to 500 meV.[20] By tight-fitting, we mean that the diffusing species at some point strongly interact with the host on two or more sides (*e.g.*, in the $LiCoO_2$ lattice; stoichiometric $LiCoO_2$ in a fully lithiated state has sluggish Li^+ diffusivity), unlike surface diffusion where the mobile species mainly interact with the host on one side. If the host framework has a large enough pore diameter > 2 Å, then this allows for the Li^+ to adsorb on the side wall of the pore, rather than be constrained at the center of a channel. Adsorption/uptake of external species is well-known in the realm of framework materials and molecular sieves. For example, zeolites have internal pore diameters ranging from $\sim$3 Å to 10 Å, which can take up large quantities of H_2O (molecular diameter 2.8 Å), H_2, and CO_2 molecules.[21] The word ''zeolite'' originated from its hygroscopicity, which literally meant ''stones that give off water steam when heated''.[22] The open aluminosilicate framework of zeolite A often gives entropic elasticity and a negative coefficient of thermal expansion (CTE) when dehydrated, which however turns positive in its fully hydrated state, when the pore is filled up.[23] Well-known framework crystals also include Prussian blue analogues (PBAs) and metal–organic frameworks (MOFs). These open frameworks often have a negative CTE, tolerance for a wide variety of molecules inside the pores, and surface-diffusion-like rapid mass transport for molecules that can fit inside the pores, making them ideal gas storage media.[24–26] Some PBAs and MOFs are even electronically conductive, making them super-MIECs.[27–29] But these large-pore open frameworks, even though generally showing diffusivity $>5 \times 10^{-13}$ m^2 s^{-1}, will not store too many alkali metal atoms per volume due to the excessively large pore sizes, and thus are not optimal for high-volumetric-energy density fast-charging electrodes.

As H_2O is the second smallest simple molecule (slightly larger than NH_3), a basic question is if it is possible to exclude molecular adsorption, while still allowing alkali ions to have surface-like adsorption and diffusion on the sidewalls of the ''internal pore surfaces'' of the framework structures. In this work, we define a pre-zeolite framework to mean crystals with percolating open pores with a diameter smaller than 2.8 Å, and therefore exclude water adsorption and generally all molecular adsorptions, while allowing surface-diffusion-like transport of Li^+. We are mainly interested in multi-valent TM-containing pre-zeolite frameworks, and will show that these frameworks, if electronically conductive, are generally all super-MIECs. We will demonstrate the structural and chemical design criteria for such pre-zeolite frameworks, in particular Wadsley–Roth structures containing multi-valent Nb, W, and Ti and having an anion-to-cation ratio (ACR) around 2.5 (mostly between 2.33 and 2.8).

While some of the compositions have been shown before, the universality and robustness of these open-pore design rules provide a cornucopia of surface-diffusion-like high-capacity super-MIECs, that would allow 10 μm sized single crystals with >30C charging/discharging rates, rivaling fossil-fuel vehicles in the charging rate.

Results and discussion

Wadsley–Roth pore with 2.5 Å < *d* < 2.8 Å is a sufficient condition for ultrafast Li^+ diffusion

We selected a representative Wadsley–Roth oxide (WRO) $H\text{-}Nb_2O_5$, and conducted first-principles calculations to clarify the physical picture of surface-like diffusion. As shown in Fig. S1a, ESI,† there are 14 open pores within the *a*–*c* plane of an $H\text{-}Nb_2O_5$ unit cell containing 28 Nb and 70 O. To study the storage and migration mechanism of Li^+ in the dilute lithiated state, we added one Li atom into a 1 × 3 × 1 supercell (containing 84 Nb and 210 O). Pore P6 (the same as *P*3 by symmetry) was picked randomly and Li^+ was placed on the interstitial site in the center of a pore surrounded by 12 O (consisting of six square planes, including two within the *a*–*c* plane perpendicular to the *b* axis and four parallel to the *b* axis on the sidewalls of the cage; see the schematic for a cubic cage in Fig. 1 where lattice distortions were neglected for simplicity). In conventional transition-metal oxides, such high-symmetry interstitial sites are typically preferred sites for Li^+ storage, for example, octahedral sites in layered $LiCoO_2$ and lithiated $Li_4Ti_5O_{12}$ ($Li_7Ti_5O_{12}$) and tetrahedral sites in spinel $LiMn_2O_4$. However, this does not apply to $H\text{-}Nb_2O_5$, whose interstitial site (pore) is so large that a pore-centered Li^+ would automatically relax to a sidewall and adopt a square planar geometry (such as sites Li^1 and Li^2 in Fig. 1(a)). We refer to such one-sided behavior as "surface adsorption" like. Such a storage mechanism has been reported in ReO_3 experimentally using the diffraction technique[30] and in Nb_2TiO_7[31] and $Nb_{12}WO_{33}$[32] by atomistic simulations.

We next used the climbing image nudged elastic band (NEB) method to calculate the migration path and energy barrier for Li^+ hopping between two neighbouring square-planar sites from one on the sidewall to the one in the *a*–*c* plane. We found the former has an energy of 130 meV lower than the latter, with a forward migration barrier of 190 meV and a backward barrier of 60 meV (Fig. S1b, ESI†). Such low barriers are surface-diffusion like, which supports the super-MIEC behavior. Yet a more striking feature is the saddle-point configuration, where the coordination number of Li^+ decreases from 4 in the square-planar ground-state (see the schematic Li^+ migration pathway from sites Li^1 to Li^2 in Fig. 1(a)) to a remarkably low coordination of 3 (marked as Li^{SD}), which is rare for lattice diffusion in crystals (The critical role of the ultra-low coordination number at the saddle point of Li^+ hopping was not realized in previous studies.[31,32]). We recall that surface diffusion can take place *via* low-coordination-number adatoms which reside on adsorption sites on the surface plane, and it does not cost much elastic energy because these adatoms can veer into the vacuum half-space (with zero moduli) instead of the solid. The analogy is thus: the saddle-point Li^+ veers into the pore with a large free volume like an adatom, and this minimizes elastic energy penalty, which typically applies to the crowded saddle-point configuration and slows down diffusion due to steric hindrance (for example, octahedral-to-tetrahedral-to-octahedral Li^+ diffusion in $LiCoO_2$). Therefore, one can justifiably call Li^+ diffusion in Wadsley–Roth $H\text{-}Nb_2O_5$ surface-like diffusion, and these "internal surfaces" are distinguishable from physical surfaces as the pores are not large enough to allow even the smallest molecules like H_2O to enter. The latter was proved by thermogravimetric analysis for wet WRO powders (Fig. S2, ESI†), where no weight loss occurred above 100 °C (surface water was mostly removed below 100 °C). Indeed, WROs have been reported as

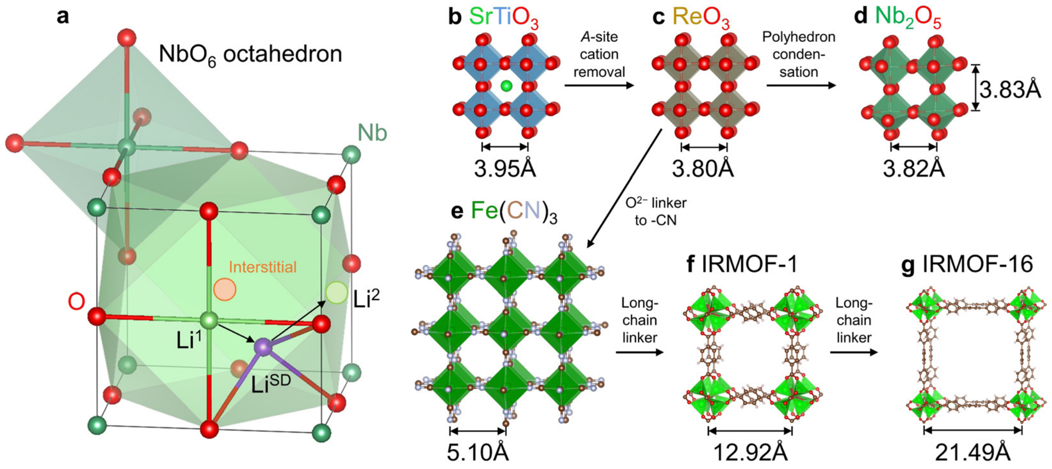

Fig. 1 Structural features of Wadsley–Roth pores. (a) Schematic Li^+ storage (sites Li^1 and Li^2) and migration pathway (from Li^1 to Li^2 *via* Li^{SD}) within a "cubic" Wadsley–Roth pore. Lattice distortions are neglected for simplicity. Structural relationship among (b) cubic $SrTiO_3$, (c) ReO_3, (d) $H\text{-}Nb_2O_5$ around the T6 tunnel, (e) Prussian blue analogue $Fe(CN)_3$, and (f) metal–organic frameworks IRMOF-1 and (g) IRMOF-16 with varying pore sizes. Marked in (b)–(g) are the cation–cation distances, which divided by $2^{1/2}$ gives the characteristic pore size. WROs are termed "pre-zeolite frameworks" due to their considerably smaller pore size than zeolites with 3–10 Å, while PBAs and MOFs may be considered as "zeolite-like" and "post-zeolite" frameworks.

bulk intercalation pseudocapacitors, and the bulk Li^+ diffusion kinetics share a similar dependence on the charge/discharge rate as the one observed for electric double-layer supercapacitors.[33]

From a crystallographic perspective, WROs are related to the ReO_3 structure[34] (Fig. 1(c), which differs from the parent perovskite structure ABO_3, *e.g.*, $SrTiO_3$ in Fig. 1(b), by removing the A-site cation) by condensing some of the corner-sharing octahedra in ReO_3 to edge-sharing ones on the boundaries of "blocks".[35] This results in better structural rigidity and d–d orbital coupling. (Compared to corner-sharing ones, edge-sharing octahedra give shorter metal–metal distance and suitable orbital orientations—d_{xy}, d_{yz}, and d_{xz} point to edge centers—for d–d coupling). Meanwhile, there are still sufficient numbers of corner-sharing octahedra inside the "blocks"[35] that form pores for Li^+ surface-like diffusion. For cubic $SrTiO_3$ and ReO_3, one may estimate the pore size by the cation–cation distance (marked in Fig. 1(b)–(g)) divided by $2^{1/2}$, thus being 2.79 Å for $SrTiO_3$ and 2.69 Å for ReO_3. A similar pore size is also noted in H-Nb_2O_5, for example, 2.70–2.71 Å for P6 (Fig. 1(d)), despite the lattice distortion and lower symmetry. Such pores allow for adatom-like Li^+ storage and internal surface-like diffusion, and are even large enough for interstitial Na^+ and K^+ storage (but not Na^+/K^+ surface-like diffusion), as cubic $NaNbO_3$ and $KNbO_3$ have cage sizes of 2.84 Å and 2.87 Å (*e.g.*, see atomic structures at materialsproject.org[36]), respectively. Therefore, the off-center Li^+ storage and Li^+ migration without steric hindrance are both verifiable, distinguishable features. Meanwhile, the framework oxygen can be replaced by other groups if large pore sizes are desired. The examples beyond LIB applications include replacing the O^{2-} for corner-sharing octahedra by $(CN)^-$ in $Fe(CN)_3$ (Fig. 1(e)) and other PBAs for Na^+ battery cathodes[37] and proton battery cathodes (H_3O^+ storage in the cage[29]), and by larger chain-molecules in mesoporous metal–organic frameworks such as IRMOF-1 (Fig. 1(f)) and IRMOF-16 (Fig. 1(g)), with varying pore sizes for gas storage and catalysis.[34] A WRO is thus identified as a pre-zeolitic framework that does not have strong hygroscopy, but can take up a large amount of Li atoms electrochemically.

The calculations above rationalize the superfast Li^+ transport in a model WRO. The insights into surface-like diffusion, as opposed to diffusion in tight-fitting channels of lithium intercalation oxides, should apply to all open pore structures with pre-zeolitic pore diameters $2.5\ \text{Å} < d < 2.8\ \text{Å}$. We thus hypothesize that the Wadsley–Roth structure by itself, with a pore channel locally similar to ReO_3, has already ensured facile bulk diffusion. Thus in real batteries, bulk diffusion in these compounds is likely not the bottleneck. The real challenge is in the boundary conditions, where side reactions and solid electrolyte interphases (SEIs) at the oxide surface build up impedance and degrade the battery during both early and prolonged cycles. As long as the $2.5\ \text{Å} < d < 2.8\ \text{Å}$ pores are maintained, we can tune the compositional space to optimize anode–electrolyte interactions to improve the cyclability. Finally, the large free volume gives rise to other structural and physical properties, such as anomalously low coefficient of thermal expansion (CTE) and formation of planar defects, which suggest soft phonon modes that could buffer strain and facilitate transport during electrochemical cycling. These shall be investigated in the following sections.

Rate parities: super-MIEC anodes with a large free volume and low CTE

We have synthesized H-Nb_2O_5, Nb_9PO_{25} (PNb_9O_{25}, NPO), a well-studied WRO Nb_2TiO_7 ($TiNb_2O_7$, NTO), a closely-related tungsten bronze structure oxide $Nb_{18}W_{16}O_{93}$ (NWO, also with a large pore size), and two new ternary oxides $Nb_9W_2Ti_6O_{40.5}$ (NWT926) and $Nb_9W_4Ti_4O_{42.5}$ (NWT944) *via* solid-state synthesis.[9,17,38,39] For all the samples, we heat-treated the powders at high temperatures (1100–1125 °C) to grow them into micron-sized single crystals. The powders obtained are phase-pure (shown by X-ray diffraction (XRD) in Fig. 2(a)) with crystal sizes shown by scanning electron microscopy (SEM) in Fig. 2(b), (c), (e) and (f). Using synchrotron powder XRD data (Fig. 2(d)), we analyzed the crystal structure of NWT926 and confirmed that it is a new phase with large pores and monoclinic symmetry (crystal structure in the inset of Fig. 2(d); data listed in Table S2, ESI†). To shed light on the free volume in the crystal lattice (critical for surface-like diffusion), we calculated the average atomic volume (defined as the supercell volume divided by the number of atoms in the supercell) of H-Nb_2O_5, NPO, NTO, NWO, and NWT926, which are in the range of 13.2–14.4 $Å^3$. The average atomic volume has been shown to correlate well with the CTE, a phonon-controlled property, and could be abnormally low or even negative in framework materials like zeolites.[40] The obtained values in our materials are close to the critical value that leads to a crossover from positive to a negative CTE (Fig. S3, ESI†). (Local average atomic volume at the pores of WROs can also be estimated from the geometry by neglecting lattice distortion and assuming a cubic ReO_3-type local structure. For example, for P6 of H-Nb_2O_5 in Fig. 1(e), it is around $3.82^3/4 = 13.9\ Å^3$.) We measured the CTEs of our powder samples using *in situ* XRD measurements (Fig. S4–S8, ESI†) conducted at 100–650 K, and the linear CTE α was obtained from the refined primary-cell volume $V_0(T)$. Compared to the CTE database for 260 compounds centered around $\sim 7 \times 10^{-6}\ K^{-1}$ (Fig. S9 and Table S3, ESI†), H-Nb_2O_5, NPO, NTO, NWO, and NWT926 indeed all have negative or close-to-zero CTEs (Fig. S4–S8, ESI†). Of particular interest is NWT926 which has negative CTEs along all three lattice axes (Fig. 2(g)), which are rare and termed triaxial negative CTEs. The reason may be that the transverse vibrations of oxygen atoms in the M–O–M (M = Nb, Ti, W) with increasing temperature lead to the rotation of corner-sharing MO_6 polyhedra, giving rise to the contraction.[24,41,42] Such anomalously low CTEs, similar to other open frameworks such as zeolites, PBAs, and MOFs, indirectly support the notion of surface-like adsorption and diffusion in all WRO super-MIECs.

We next measured the electrochemical performances of H-Nb_2O_5, NPO, NWT926, and NWT944 as LIB anodes in half cells and compared them with NTO and NWO references. By definition, super-MIEC materials should have high intrinsic electronic conductivity to assist electronic percolation. Therefore, we minimized the usage of conductive carbon in the composite electrode and tested all the anodes with >85 wt% active materials. At a low

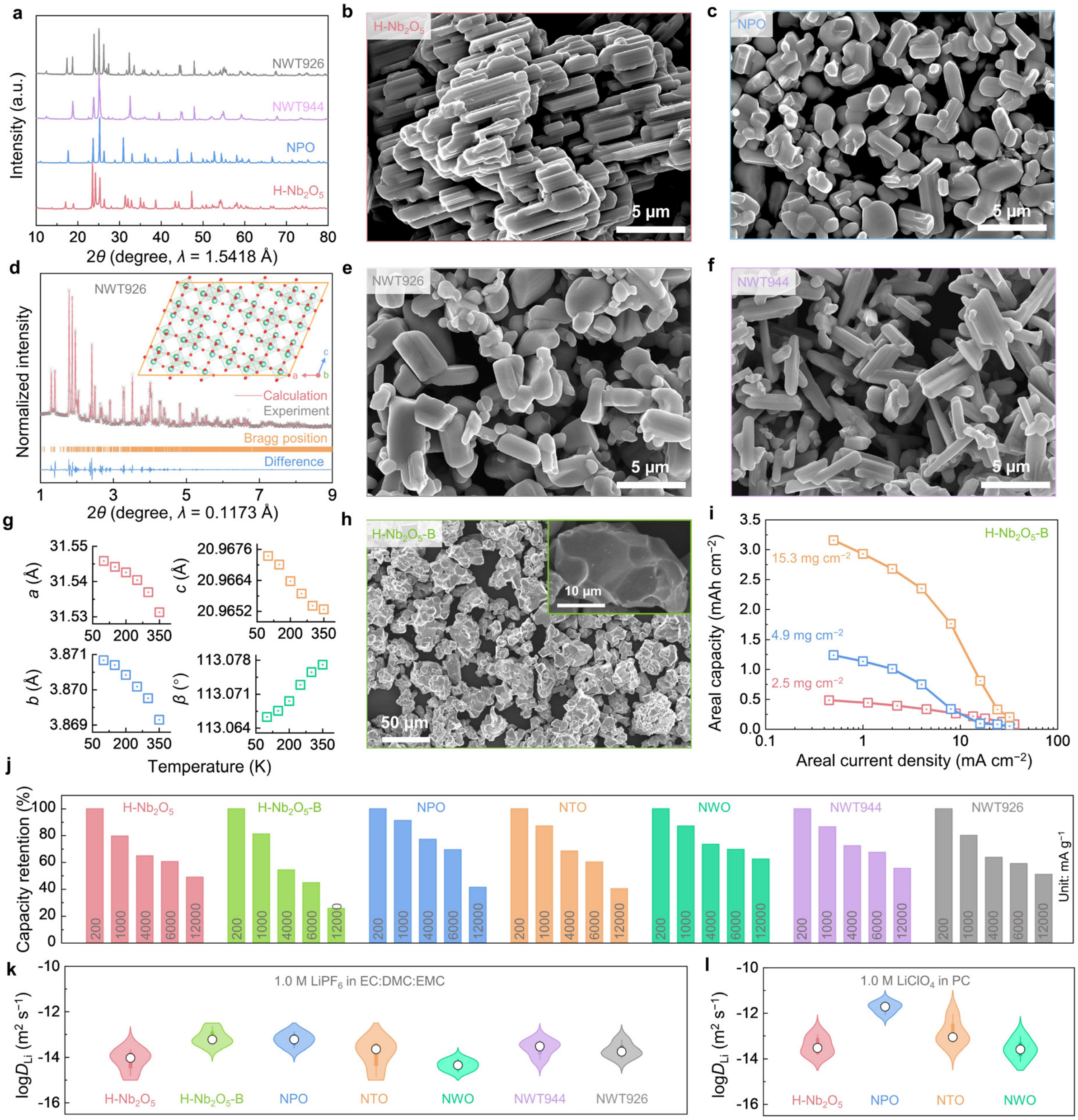

Fig. 2 Structural characterization and electrochemical performances of super-MIEC anodes. (a) XRD patterns of H-Nb_2O_5, NPO, NWT944 and NWT926. SEM images of (b) H-Nb_2O_5, (c) NPO, (e) NWT926, (f) NWT944, and (h) H-Nb_2O_5-B. (d) The high-energy synchrotron diffraction pattern and the refinement analysis of NWT926, and the inset shows the structural illustration of the new phase. (g) Primary-cell parameters as a function of temperature T of NWT926. (i) The effect of current densities and mass loadings on the areal capacities of H-Nb_2O_5-B. (j) Capacity retention at different rates and (k), (l) electrochemically measured D_{Li} of H-Nb_2O_5, H-Nb_2O_5-B, NPO, NTO, NWO, NWT944 and NWT926.

rate of 200 mA g^{-1} and a lower cutoff voltage of 1.0 V (*vs.* Li^+/Li), H-Nb_2O_5, NPO, NTO, NWO, NWT926, and NWT944 have specific capacities of 192 mA h g^{-1}, 210 mA h g^{-1}, 236 mA h g^{-1}, 180 mA h g^{-1}, 187 mA h g^{-1}, and 204 mA h g^{-1}, respectively. They all have suitable average voltage (1.5–1.7 V *vs.* Li^+/Li), high Coulombic efficiency (CE), and a stable charge–discharge profile upon cycling (Fig. S10–S12, ESI†). When tested at higher rates (for both charge and discharge) up to 16 000 mA g^{-1} (roughly 200∼300C), we found all six materials have good capacity retention (for the capacity at 200 mA g^{-1}, Fig. 2(j)). At 6000 mA g^{-1}, the capacity retentions are >50%, offering 116 mA h g^{-1} capacity for H-Nb_2O_5, 146 mA h g^{-1} for NPO, 142 mA h g^{-1} for NTO, 125 mA h g^{-1} for NWO, 110 mA h g^{-1} for NWT926, and 138 mA h g^{-1} for NWT944. These correspond to ∼60C, which would satisfy many high-rate applications, shifting the rate-limiting consideration to the cathode or electrolyte in the full cells.

D_{Li} is the composite of the Li^+ ion and e^- polaron diffusivities in ambipolar diffusion theory. First, the electronic conductivities of Nb_2O_5 and $Li_{0.1}Nb_2O_5$ were calculated to be 1.0×10^{-6} S m^{-1}, and 6.6 S m^{-1}, respectively, by measuring the 2-probe electronic resistance, area, and thickness of the pellet

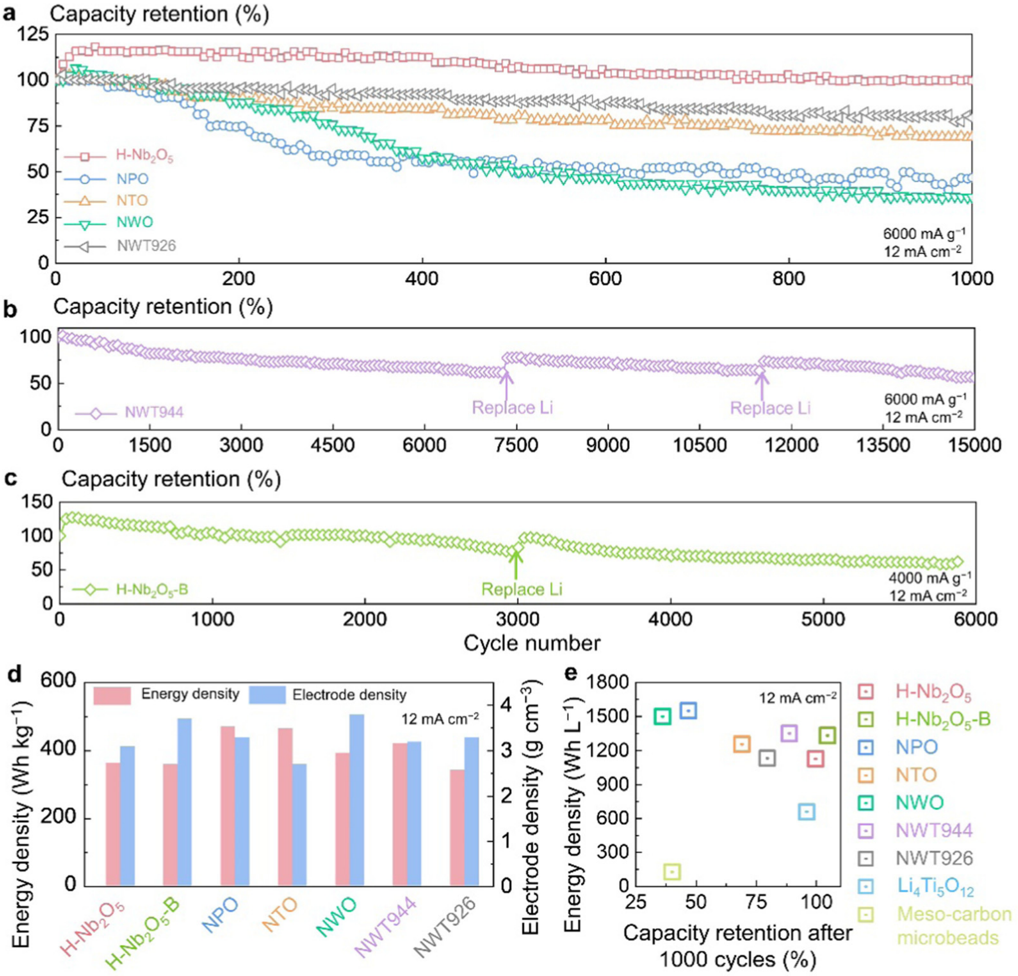

Fig. 3 Cyclability comparison among the Super-MIEC anodes. Capacity retention of (a) H-Nb_2O_5, NPO, NTO, NWO, NWT926, and (b) NWT944 at 6000 mA g^{-1}, and (c) capacity retention of H-Nb_2O_5-B at 4000 mA g^{-1}. (d) Gravimetric energy density and electrode density of super-MIEC anodes including H-Nb_2O_5, H-Nb_2O_5-B, NPO, NTO, NWO, NWT944, and NWT926. (e) Volumetric energy density and capacity retention of super-MIEC anodes including H-Nb_2O_5, H-Nb_2O_5-B, NPO, NTO, NWO, NWT944, NWT926, $Li_4Ti_5O_{12}$ and meso-carbon microbeads.

samples. Therefore, slightly lithiated Nb_2O_5 can be regarded as a good electronic conductor. To enable facile kinetics at 60C for ~1 μm single crystals, D_{Li} needs to be ~10^{-14} m^2 s^{-1}. To verify, galvanostatic intermittent titration technique (GITT) measurements (Fig. S13, ESI†) were conducted at different states of charge and at temperatures of 10–50 °C relevant for LIB operations. As shown by the violin plots in Fig. 2(k), D_{Li} values from GITT measurements are within the range of 10^{-15}–10^{-12} m^2 s^{-1} for all the anodes. These values are comparable to the D_{Li} values of 10^{-16}–10^{-12} m^2 s^{-1} in famous cathodes of $LiCoO_2$ and $LiNi_{0.33}Co_{0.33}Mn_{0.33}O_2$ (Fig. S14, ESI,† similarly calculated from GITT measurements). The measurements above were from half cells using ethylene carbonate (EC)-based electrolytes. Interestingly, when we switched to propylene carbonate (PC)-based electrolytes, H-Nb_2O_5, NPO, NTO, and NWO showed 1–2 orders of magnitude higher D_{Li} (Fig. 2(l) and Fig. S15, ESI†) than their respective values measured by the GITT in EC-based ones. It suggests that the measured diffusivities may not be the intrinsic ones in the crystal lattice but are likely to be constrained by SEIs formed during electrochemical tests. This inspires us to further modify the morphology and grow larger single crystals with less electrochemically active surfaces. We have made successful attempts to grow H-Nb_2O_5 in ~20 μm-sized particles (abbreviated as H-Nb_2O_5-B; XRD in Fig. S16c, ESI;† SEM in Fig. 2(h) and a particle size analyzer in Fig. S16d, ESI† were used to obtain an agglomeration size of D_{50} = 49.0 μm) and again tested its electrochemical performance (216 mA h g^{-1} capacity at 200 mA g^{-1}, Fig. S16b, ESI†). Remarkably, H-Nb_2O_5-B shows superior rate capability at different mass loadings (Fig. 2(i)), which is similar to H-Nb_2O_5 (Fig. 2(j)), despite ~10 times larger grain size, and it can deliver an impressive capacity of 110 mA h g^{-1} at 6000 mA g^{-1} (~60C). The D_{Li} value of H-Nb_2O_5-B from GITT measurements is also >10 times larger than H-Nb_2O_5. Therefore, we conclude that WROs have high D_{Li} in electrochemical cells and superior rate performance, which is relatively insensitive to oxide compositions but more sensitive to SEIs. The formation and growth of SEIs depend on the electro-chemo-mechanical interactions between active electrode materials and the electrolytes, which affect the rate capability and cycling stability of the anode and the full cell.

Cyclability disparities: towards the long cycle life of high-rate LIBs

High-rate LIBs require an extended cycle life, and >10 000 cycle life has been demonstrated by the $LiFePO_4$ cathode and $Li_4Ti_5O_{12}$ anode. We therefore evaluated the cycling stability of the synthesized super-MIEC anodes in half cells (*i.e.*, with excess electrolyte and Li reservoir). As shown in Fig. 3(a), when cycled at 6000 mA g^{-1} (12 mA cm^{-2}, ~60C), NTO, NPO, and NWO rapidly decay and have capacity retentions of 69%, 47%, and 36% after 1000 cycles, respectively. H-Nb_2O_5 and NWT926 have better cycling stability, with 100% and 80% capacity retentions after 1000 cycles. In comparison, NWT944 shows remarkably improved stability (Fig. 3(b)), with 62% capacity retention after 7000 cycles (5.4% decay per 1000 cycles). To exclude capacity decay drivers from the other battery components, we replaced the Li metal counter electrode and the electrolytes after 7300 and 11 500 cycles (severe degradation of the Li metal electrode is shown in Fig. S17, ESI†). 56% capacity retention over 15 000 cycles has thus been achieved in NWT944. On the other hand, by tailoring the morphology and increasing the particle size, we show in Fig. 3(c) that H-Nb_2O_5-B has 5% higher capacity after 1000 cycles than its initial capacity (attributed to the activation process occurring in electrochemical cycling[43]), and it also has capacity retentions of 77% after 3000 cycles, and 60% after 5800 cycles when cycled at 4000 mA g^{-1} (similar areal current density of 12 mA cm^{-2}), representing improvements over H-Nb_2O_5. Therefore, our new composition (NWT944) and crystal size-coarsened H-Nb_2O_5-B both demonstrate a superior cycle life compared with previous WROs[9,12,17–19,44–48] (Table S1, ESI†). With suitable coatings and electrolyte modifications, we believe extended cycle life can be realized in full cells in all WROs, as the lattice volume change is small. (Preliminary investigations

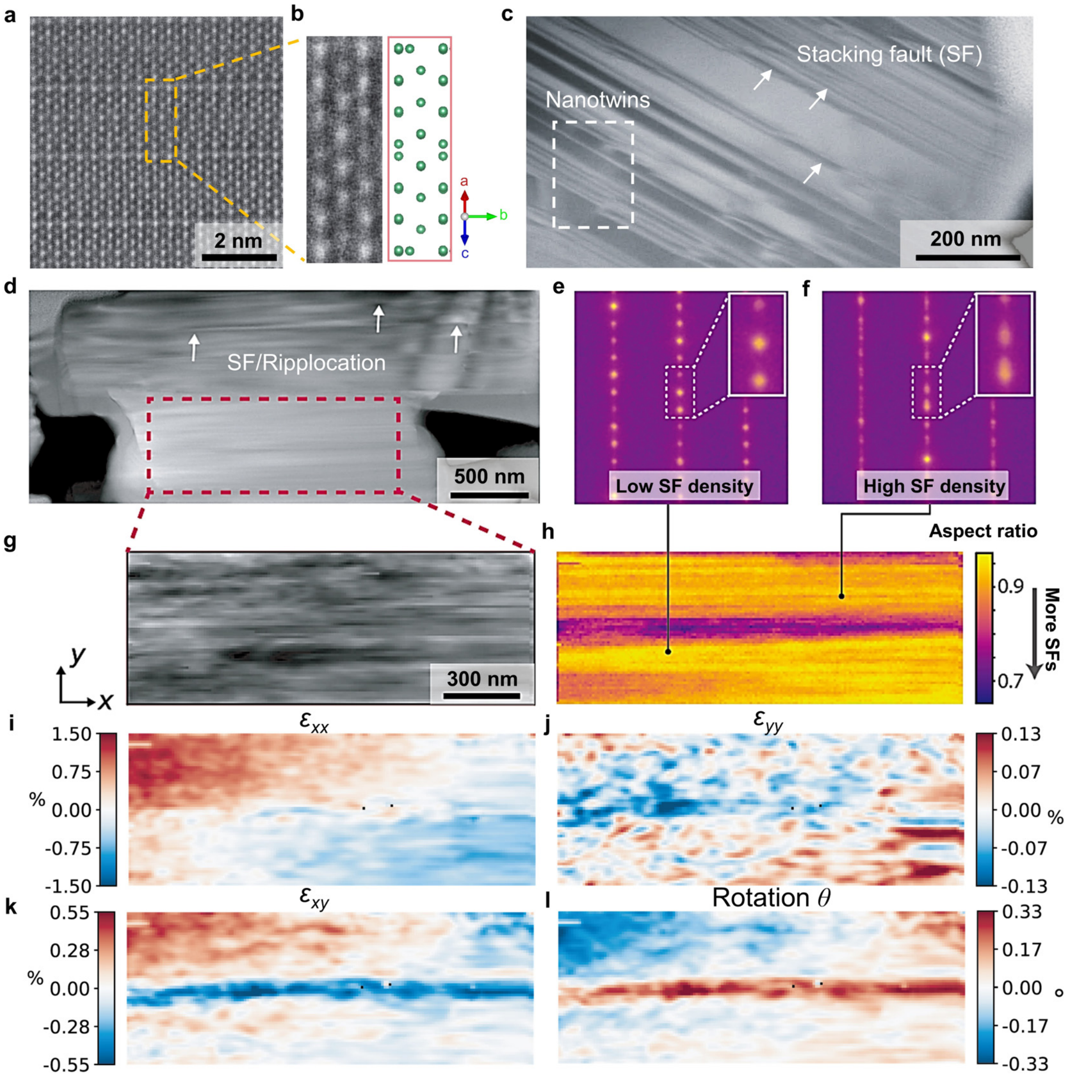

Fig. 4 Lattice-structural features of Super-MIEC anodes. (a) High-resolution scanning transmission electron microscopy-high-angle annular dark-field (STEM-HAADF) image of H-Nb_2O_5 as well as (b) the corresponding crystal structure. (c), (d), and (g) Low-magnification STEM-HAADF images showing the focused ion beam (FIB) lift-out transmission electron microscopy (TEM) foil of H-Nb_2O_5. (e) and (f) Nanobeam electron diffraction patterns showing the spatial fluctuations in the SF density of the selected area of (h). 4D-STEM lattice strain mapping of components (i) ε_{xx}, (j) ε_{yy}, and (k) ε_{xy}, and (l) lattice rotation angle θ within the x–y plane.

have been conducted in coin-type full cells using the H-Nb_2O_5 anode paired with the $LiNi_{0.5}Mn_{1.5}O_4$ or $LiFePO_4$ cathode, and in pouch-type full cells using the H-Nb_2O_5 anode paired with the $LiNi_{0.6}Co_{0.2}Mn_{0.2}O_2$ cathode and the H-Nb_2O_5-B anode paired with the $LiCoO_2$ cathode, as shown in Fig. S18, ESI†).

Super-MIEC anodes compete with $Li_4Ti_5O_{12}$ in high-rate applications. We compared the gravimetric energy density and electrode density of super-MIEC anodes in Fig. 3(d), which gives volumetric energy density in the range of $1128 \sim 1550$ W h L^{-1} (at 6000 mA g^{-1}, Fig. 3(e)) with the rank of NPO > NWO > NWT944 > H-Nb_2O_5-B > NTO > NWT926 > H-Nb_2O_5. (More detailed comparisons on characterized particle size, electrode density, initial Coulombic efficiency, capacity, rate retention, average voltage, energy density, and cyclability are listed in Tables S4 and S5, ESI†.) These values are much higher than 658 W h L^{-1} for $Li_4Ti_5O_{12}$ and 127 W h L^{-1} for meso-carbon microbeads, which are the commercially prevailing high-rate anodes. Through trial and error, it appears that Nb is the baseline element to form the Wadsley–Roth oxide structure, W is beneficial for increasing the crystal density and energy density, and Ti is beneficial for enhancing the structural stability. We note that in many applications, the cycle life is an important metric, which sets NWT944 and H-Nb_2O_5-B to be the best candidates among the super-MIEC anodes investigated.

Other lattice-structural and microstructural features

As an anode must host and disgorge a great amount of excess lithium reversibly, a robust atomic structure is required. As shown by the top surfaces and cross-sections of H-Nb_2O_5, NPO, and NWT944 electrodes (Fig. S19, ESI†), the single-crystal WRO particles did not fracture after cycling. This means the particles could survive the mechanical stresses and stress-corrosion cracking during cyclic electrochemical loading, which would benefit the long-term cycling stability. Indeed, the scanning

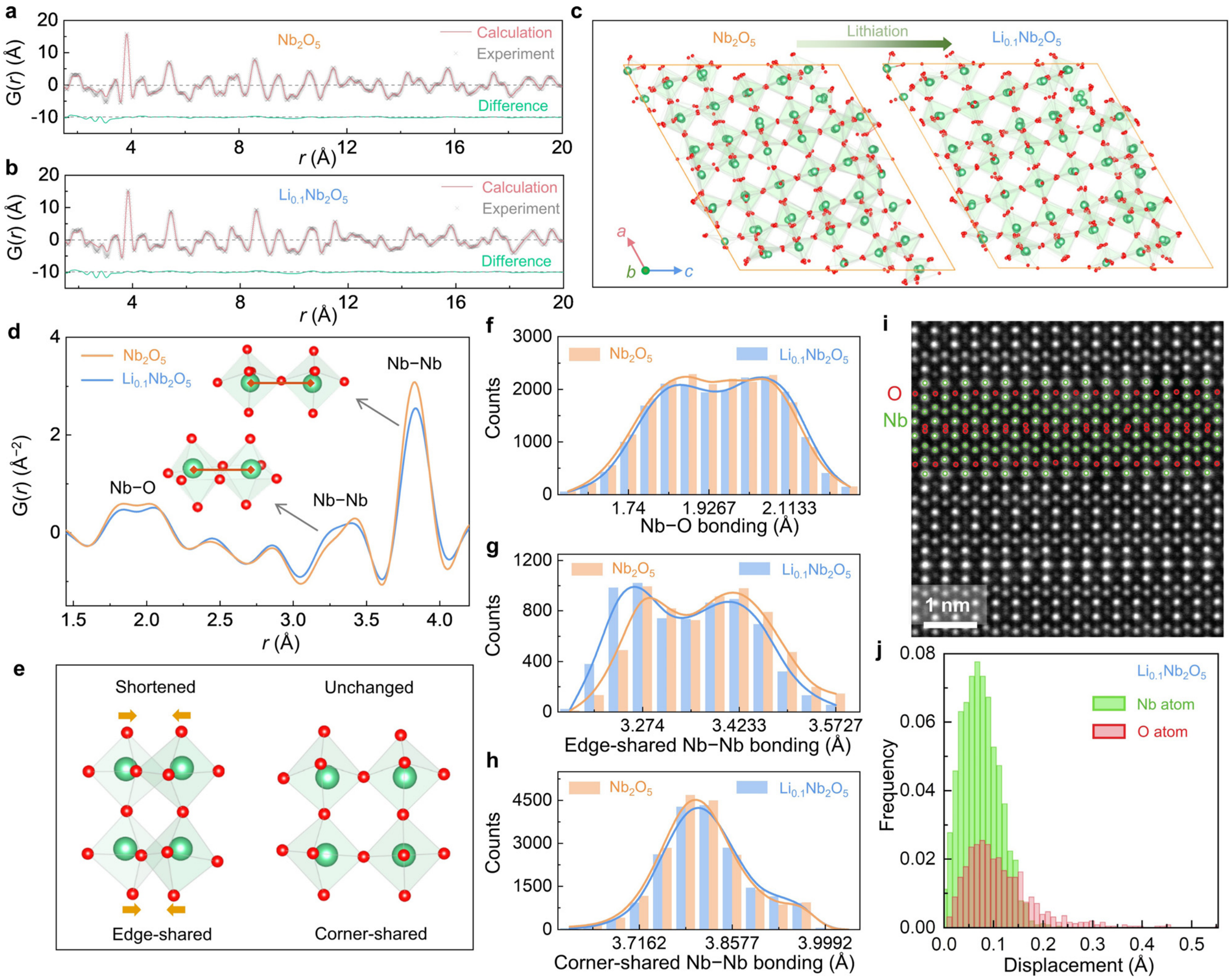

Fig. 5 Microstructural features of Super-MIEC anodes. Pair distribution function (PDF) measurements as well as Reverse Monte Carlo (RMC) simulation for (a) Nb_2O_5 and (b) $Li_{0.1}Nb_2O_5$. (c) Structural comparison between Nb_2O_5 and $Li_{0.1}Nb_2O_5$ by using the results of RMC simulation. (d) Comparison of original PDF experimental data and (e) schematic diagram of the structural changes before and after lithiation. Comparison of bonding lengths of (f) Nb–O, (g) edge-sharing Nb–Nb, and (h) corner-sharing Nb–Nb of Nb_2O_5 and $Li_{0.1}Nb_2O_5$. (i) Variable-angle HAADF image in scanning transmission electron microscopy as well as the (j) distribution of displacement for $Li_{0.1}Nb_2O_5$.

transmission electron microscopy – high-angle annular dark-field (STEM-HAADF) image in Fig. 4(a) shows well-ordered crystal lattices without point defects (corresponding atomic structure for the Nb sublattice in Fig. 4(b)).

However, over a larger length scale of a few hundred nanometers, extended defects including stacking faults, nanotwins, and ripplocations[49] were found in the WRO single crystals (Fig. 4(c), (d) and Fig. S20, ESI†). Different levels of diffuse scattering exist in the nanobeam electron diffraction patterns (Fig. 4(e) and (f)) at different locations of Fig. 4(d), and mapping of stacking fault density in Fig. 4(g) and (h) further indicates spatial variations. As these planar defects are formed in pristine H-Nb_2O_5 synthesized from high-temperature heat treatment, the observations indicate their relatively low formation energies. It is in contrast with the high formation energy of point defects, but consistent with the fact that the large free volume and low CTE in WROs are a result of low polyhedral packing density and their collective twisting/relaxation. In addition, strain mapping by four-dimensional scanning transmission electron microscopy (4D-STEM) at 10 nm spatial resolution (Fig. 4(g)) visualizes the lattice at the mesoscale, with a standard deviation of 1.53% for ε_{xx}, 1.44% for ε_{yy}, 0.20% for ε_{xy}, and 0.12% for the rotation angle θ (Fig. 4(i)–(l)).

Pair distribution function (PDF) analysis was conducted on unlithiated (Nb_2O_5 in Fig. 5(a)) and slightly lithiated ($Li_{0.1}Nb_2O_5$ in Fig. 5(b)) H-Nb_2O_5 powders using synchrotron X-ray total scattering. Experimentally, the raw total scattering data were collected and then transformed into the real-space PDF $G(r)$.[50,51] For Nb_2O_5, we noted the measured $G(r)$ significantly deviates from the calculated one from the "perfect" H-Nb_2O_5 structure (Fig. 1(a)), especially at large r up to 20 Å. We thus conducted reverse Monte Carlo (RMC) simulations to fit the experimental data (calculated $G(r)$ shown in Fig. 5(a), (b)) and to analyze the structure. As shown by simulated atomic structures (Fig. 5(c)) after converged RMC simulations, there are distortions at both Nb and O sublattices, even though O displacements (average value 0.06 Å for Nb_2O_5 and 0.05 Å for $Li_{0.1}Nb_2O_5$) are larger than Nb displacements (average value 0.01 Å for Nb_2O_5 and 0.01 Å for $Li_{0.1}Nb_2O_5$, Fig. S21, ESI†). To compare the structure before and after lithiation, we focused on $G(r)$ data at 1.5∼4.0 Å (Fig. 5(d)), especially the ∼1.9 Å double peaks for nearest Nb–O bonds, the ∼3.3 Å double peaks for nearest Nb–Nb bonds for edge-sharing NbO_6 octahedra, and the ∼3.8 Å peak for Nb–Nb bonds for corner-sharing NbO_6 octahedra. When lithiating from Nb_2O_5 to $Li_{0.1}Nb_2O_5$, we found minimum changes in ∼1.9 Å Nb–O bonds (Fig. 5(f)) and ∼3.8 Å Nb–Nb bonds (Fig. 5(h)) but shortened Nb–Nb bonds at ∼3.3 Å (Fig. 5(g)). It indicates the pore structure is relatively robust and does not involve much structural change upon lithiation. To confirm, we conducted STEM-HAADF on $Li_{0.1}Nb_2O_5$, which provides contrasts for light-element O. As shown in Fig. 5(i), the lattice is again well ordered, yet slight distortions on the O sublattice are notable. Quantitative analysis of the atomic positions (Fig. 5(j)) shows 0.004 Å (with a standard deviation of 0.008 Å) displacements in the Nb sublattice and 0.02 Å (with a standard deviation of 0.02 Å) displacements in the O sublattice, and some O atoms are displaced further up to ∼0.45 Å. These results agree with the diffraction and RMC data.

Lastly, we used *in situ* XRD to measure the CTEs of lithiated H-Nb_2O_5 at 100–200 K (Fig. S22 and S23, ESI†). Interestingly, negative CTEs of $-8.80 \times 10^{-6}\ K^{-1}$ and $-4.21 \times 10^{-6}\ K^{-1}$ were obtained for $Li_{0.2}Nb_2O_5$ and $Li_{1.6}Nb_2O_5$, respectively, which are lower than that of $-0.53 \times 10^{-6}\ K^{-1}$ for non-lithiated H-Nb_2O_5. This again suggests that the large free volume holds even upon electrochemical lithiation.

Conclusions and outlook

We have explained why the WROs have fast Li^+ diffusion ability and abnormally low CTEs. The low topological constraints per atom and large free volume in the crystal lattice should be the fundamental cause of soft phonons, low CTE, low-coordination-number Li^+ storage, and surface-like diffusion, similar to other open frameworks such as zeolites, PBAs, and MOFs. But unlike those frameworks that take up molecules, the WRO frameworks with $2.5\ Å < d < 2.8\ Å$ can only take up atoms like Li. The phonon anomalies are expected to influence the pre-exponential factor of the Arrhenius-type diffusivity. There is literature on D_{Li} measured by pulsed-field-gradient nuclear magnetic resonance (PFG NMR) spectroscopy, which is a bulk measurement and not sensitive to SEIs. In Fig. S2a, ESI† of ref. 9, in $Li_xNb_yW_zO_{(5y+6z)/2}$, we note that larger activation energy gives higher D_{Li} values, because a large pre-exponential term not only compensates but also dominates (Table S6, ESI†), signifying perhaps collective Li motion in pores.

Another question is why Nb (group-5, period-5) is essential in forming WRO super-MIEC anodes. Turning back to the parent structure ReO_3, partial condensation of the corner-sharing octahedra to edge-sharing ones is necessary to enhance the structural rigidity (to suppress extensive phase transitions during electrochemical cycling; unalloyed ReO_3 has multiple phase transitions upon lithiation, which leads to slow kinetics, voltage hysteresis, and poor cycling[52]) and d–d coupling for better electron transport. Therefore, an ACR around 2.5 is expected, which requires a +5 average cation valence, and thus group-5 elements (Zr/Hf likes to be +4, Mo/W likes to be +6). Meanwhile, as the octahedron majority should be maintained, the fact—that V^{5+} is so small that it prefers to be coordinated by four neighboring O^{2-} as is the case for various V_2O_5 polymorphs; while Ta^{5+} is so large that it prefers mixed TaO_6/TaO_7 occupancy as is the case for L- and H-Ta_2O_5—sets group-5 and period-5 Nb^{5+} to be the best candidate for the major cation. Other elements (Ti, W) can be alloyed into the lattice, to tune the bulk redox and surface stability.

Finally, we provide some guidance on the search for other candidates in the multi-element compositional space. As Roth and Wadsley categorized, the "block" structured oxides M_xO_y can be represented by a series of chemical formulas with one single integer variable n, including $M_{3n}O_{8n-3}$ for Group A, $M_{3n+1}O_{8n-2}$ (n odd) for Group B, $M_{3n+1}O_{8n-2}$ (n even) for Group C, $M_{3n+1}O_{8n+1}$ for Group D, $M_{4n+1}O_{11n}$ for Group E, and

$M_{5n+1}O_{14n-1}$ for Group F.[35,53] Taking the limiting cases as $n \to \infty$ and known small n compositions (*e.g.*, $n = 3$ for Nb_2TiO_7 in Group A, $n = 7$ for $Nb_{22}O_{54}$ in Group B, $n = 8$ for $Nb_{24}TiO_{62}$ in Group C, $n = 3$ for Nb_9TPO_{25} in Group D, $n = 3$ for $Nb_{12}WO_{33}$ in Group E, and $n = 4$ for $Nb_{16}W_5O_{55}$ in Group F), we obtained the O/M ratio in the range of 2.33–2.8. Applying such boundaries to the $NbO_{2.5}$–WO_3–TiO_2 ternary phase diagram offers the potential compositional ranges to synthesize new WROs (Fig. S24, ESI†) to optimize bulk redox and SEIs. Indeed, all the known materials within this category fall into the colored compositional space, including our newly synthesized NWT944 and NWT926. The O/M = 2.5 tie-line is of particular interest, which is achieved by alloying WO_3 and TiO_2 with a 1 : 1 molar ratio into the $NbO_{2.5}$ matrix. This, together with the coarsened crystal size and suitable coatings, enables the prolonged cycle lives of super-MIEC anodes in high-rate LIBs.

Author contributions

S. W., L. Z., Y. D., J. Z., Z. T., and J. L. conceived the project. L. Z. synthesized the materials and conducted electrochemical testing. H. Z. and H. X. contributed to the PDF analysis and RMC simulation. H. W. and Y. D. conducted the bond-valence sum simulations and first-principles calculations. Y. Yang, B. W., Y. S., and A. M. contributed to the FIB sample preparation, spherical aberration TEM and atomic resolution STEM-HAADF imaging, and 4D-STEM characterization and stacking fault mapping analysis. Y. Yuan and Q. H. contributed to the displacement analysis of the HAADF image. S. W. and Y. H. analyzed the GITT data. H. Z., Q. L., Y. R., C. S., and Q. L. contributed to the synchrotron measurement for structural analysis and CTE analysis. R. F. contributed to Li nuclear magnetic resonance measurements confirming ultrafast Li^+ diffusion. X. H., Y. C., X. X., and W. L. contributed to the X-ray scanning nano-diffraction measurements. W. Q., Y. L., Z. X., and Z. Z. contributed to the pouch cells assembling and measurement. S. W., Y. D., and J. L. wrote the paper. All authors discussed and contributed to the writing.

Conflicts of interest

The authors declare that they have no competing interests.

Acknowledgements

J. Z. acknowledges the support from the State Key Laboratory of New Ceramic and Fine Processing, Tsinghua University (No. KF201801). Z. T. acknowledges support from the National Natural Science Foundation of China (No. 51772163, 52172210). J. L. acknowledges the support from Honda Research Institute USA, Inc. Y. Y. was supported by the Director, Office of Science, Office of Basic Energy Sciences, Materials Sciences and Engineering Division, the U.S. Department of Energy under contract no. DE-AC02-05-CH11231 within the Mechanical Behavior of Materials (KC 13) program at the Lawrence Berkeley National Laboratory. A. M. was supported by the Toyota Research Institute. The authors acknowledge support from the Molecular Foundry at Lawrence Berkeley National Laboratory, which is supported by the U.S. Department of Energy under contract no. DE-AC02-05-CH11231. This research used resources of the Advanced Photon Source, a U.S. Department of Energy (DOE) Office of Science user facility operated for the DOE Office of Science by Argonne National Laboratory under contract no. DE-AC02-06CH11357. Q. L. acknowledges the Shenzhen Science and Technology Innovation Commission under grant SGDX2019081623240948. X. H acknowledges the support from the U.S. Department of Energy under contract no. DE-SC0012704. R. F. acknowledges the support from the NSF Cooperative Agreement DMP-1644779 and the State of Florida.

References

1 Y. Chen, Z. Wang, X. Li, X. Yao, C. Wang, Y. Li, W. Xue, D. Yu, S. Y. Kim, F. Yang, A. Kushima, G. Zhang, H. Huang, N. Wu, Y. W. Mai, J. B. Goodenough and J. Li, *Nature*, 2020, **578**, 251–255.
2 A. Sood, A. D. Poletayev, D. A. Cogswell, P. M. Csernica, J. T. Mefford, D. Fraggedakis, M. F. Toney, A. M. Lindenberg, M. Z. Bazant and W. C. Chueh, *Nat. Rev. Mater.*, 2021, **6**, 847–867.
3 P. C. Harikesh, A. Surendran, B. Ghosh, R. A. John, A. Moorthy, N. Yantara, T. Salim, K. Thirumal, W. L. Leong, S. Mhaisalkar and N. Mathews, *Adv. Mater.*, 2020, **32**, 1906976.
4 I. Riess, *Solid State Ionics*, 2003, **157**, 1–17.
5 H. Sun, L. Mei, J. Liang, Z. Zhao, C. Lee, H. Fei, M. Ding, J. Lau, M. Li, C. Wang, X. Xu, G. Hao, B. Papandrea, I. Shakir, B. Dunn, Y. Huang and X. Duan, *Science*, 2017, **356**, 599–604.
6 Y. Liu, Y. Zhu and Y. Cui, *Nat. Energy*, 2019, **4**, 540–550.
7 H. Liu, Z. Zhu, Q. Yan, S. Yu, X. He, Y. Chen, R. Zhang, L. Ma, T. Liu, M. Li, R. Lin, Y. Chen, Y. Li, X. Xing, Y. Choi, L. Gao, H. S.-Y. Cho, K. An, J. Feng, R. Kostecki, K. Amine, T. Wu, J. Lu, H. L. Xin, S. P. Ong and P. Liu, *Nature*, 2020, **585**, 63–67.
8 W. Zhang, D. H. Seo, T. Chen, L. Wu, M. Topsakal, Y. Zhu, D. Lu, G. Ceder and F. Wang, *Science*, 2020, **367**, 1030–1034.
9 K. J. Griffith, K. M. Wiaderek, G. Cibin, L. E. Marbella and C. P. Grey, *Nature*, 2018, **559**, 556–563.
10 Y. Li, S. Wang, Y. Dong, Y. Yang, Z. Zhang and Z. Tang, *Adv. Energy Mater.*, 2019, **10**, 1903411.
11 S. T. Wang, Y. H. Dong, F. J. Cao, Y. T. Li, Z. T. Zhang and Z. L. Tang, *Adv. Funct. Mater.*, 2020, **30**, 2001026.
12 B. Babu, P. Simon and A. Balducci, *Adv. Energy Mater.*, 2020, **10**, 2001128.
13 Q. Ai, Q. Fang, J. Liang, X. Xu, T. Zhai, G. Gao, H. Guo, G. Han, L. Ci and J. Lou, *Nano Energy*, 2020, **72**, 104657.
14 S. Wang, W. Quan, Z. Zhu, Y. Yang, Q. Liu, Y. Ren, X. Zhang, R. Xu, Y. Hong, Z. Zhang, K. Amine, Z. Tang, J. Lu and J. Li, *Nat. Commun.*, 2017, **8**, 627.
15 C. Choi, D. S. Ashby, D. M. Butts, R. H. DeBlock, Q. Wei, J. Lau and B. Dunn, *Nat. Rev. Mater.*, 2019, **5**, 5–19.
16 T. Yuan, Z. Tan, C. Ma, J. Yang, Z.-F. Ma and S. Zheng, *Adv. Energy Mater.*, 2017, **7**, 1601625.

17 Y. Yang and J. Zhao, *Adv. Sci.*, 2021, **8**, 2004855.

18 Q. Deng, Y. Fu, C. Zhu and Y. Yu, *Small*, 2019, **15**, 1804884.

19 K. J. Griffith, Y. Harada, S. Egusa, R. M. Ribas, R. S. Monteiro, R. B. Von Dreele, A. K. Cheetham, R. J. Cava, C. P. Grey and J. B. Goodenough, *Chem. Mater.*, 2020, **33**, 4–18.

20 Z. Liu and X. Huang, *Solid State Ionics*, 2010, **181**, 907–913.

21 N. Rangnekar, N. Mittal, B. Elyassi, J. Caro and M. Tsapatsis, *Chem. Soc. Rev.*, 2015, **44**, 7128–7154.

22 C. J. Jacobsen, C. Madsen, J. Houzvicka, I. Schmidt and A. Carlsson, *J. Am. Chem. Soc.*, 2000, **122**, 7116–7117.

23 T. Carey, C. C. Tang, J. A. Hriljac and P. A. Anderson, *Chem. Mater.*, 2014, **26**, 1561–1566.

24 Q. Gao, J. Chen, Q. Sun, D. Chang, Q. Huang, H. Wu, A. Sanson, R. Milazzo, H. Zhu, Q. Li, Z. Liu, J. Deng and X. Xing, *Angew. Chem., Int. Ed.*, 2017, **56**, 9023–9028.

25 Z. Chang, D. H. Yang, J. Xu, T. L. Hu and X. H. Bu, *Adv. Mater.*, 2015, **27**, 5432–5441.

26 J. Li, P. M. Bhatt, J. Li, M. Eddaoudi and Y. Liu, *Adv. Mater.*, 2020, **32**, 2002563.

27 L. S. Xie, G. Skorupskii and M. Dinca, *Chem. Rev.*, 2020, **120**, 8536–8580.

28 K. Hurlbutt, S. Wheeler, I. Capone and M. Pasta, *Joule*, 2018, **2**, 1950–1960.

29 X. Y. Wu, J. J. Hong, W. Shin, L. Ma, T. C. Liu, X. X. Bi, Y. F. Yuan, Y. T. Qi, T. W. Surta, W. X. Huang, J. Neuefeind, T. P. Wu, P. A. Greaney, J. Lu and X. L. Ji, *Nat. Energy*, 2019, **4**, 123–130.

30 R. J. Cava, A. Santoro, D. W. Murphy, S. M. Zahurak and R. S. Roth, *J. Solid State Chem.*, 1983, **50**, 121–128.

31 K. J. Griffith, I. D. Seymour, M. A. Hope, M. M. Butala, L. K. Lamontagne, M. B. Preefer, C. P. Kocer, G. Henkelman, A. J. Morris, M. J. Cliffe, S. E. Dutton and C. P. Grey, *J. Am. Chem. Soc.*, 2019, **141**, 16706–16725.

32 C. P. Kocer, K. J. Griffith, C. P. Grey and A. J. Morris, *Chem. Mater.*, 2020, **32**, 3980–3989.

33 Y. Liu, S. P. Jiang and Z. Shao, *Mater. Today Adv.*, 2020, **7**, 100072.

34 H. A. Evans, Y. Wu, R. Seshadri and A. K. Cheetham, *Nat. Rev. Mater.*, 2020, **5**, 196–213.

35 R. Roth and A. Wadsley, *Acta Crystallogr.*, 1965, **19**, 42–47.

36 S. P. Ong, A. Jain, G. Hautier, B. Kang and G. Ceder, *Electrochem. Commun.*, 2010, **12**, 427–430.

37 Q. N. Liu, Z. Hu, M. Z. Chen, C. Zou, H. L. Jin, S. Wang, S. L. Chou, Y. Liu and S. X. Dou, *Adv. Funct. Mater.*, 2020, **30**, 1909530.

38 L. Zhao, S. Wang, Y. Dong, W. Quan, F. Han, Y. Huang, Y. Li, X. Liu, M. Li, Z. Zhang, J. Zhang, Z. Tang and J. Li, *Energy Storage Mater.*, 2021, **34**, 574–581.

39 T. Li, G. Nam, K. Liu, J.-H. Wang, B. Zhao, Y. Ding, L. Soule, M. Avdeev, Z. Luo, W. Zhang, T. Yuan, P. Jing, M. G. Kim, Y. Song and M. Liu, *Energy Environ. Sci.*, 2022, **15**, 254–264.

40 Q. Gao, J. Wang, A. Sanson, Q. Sun, E. Liang, X. Xing and J. Chen, *J. Am. Chem. Soc.*, 2020, **142**, 6935–6939.

41 Z. Liu, Q. Li, H. Zhu, K. Lin, J. Deng, J. Chen and X. Xing, *Chem. Commun.*, 2018, **54**, 5712–5715.

42 Q. Gao, N. Shi, Q. Sun, A. Sanson, R. Milazzo, A. Carnera, H. Zhu, S. H. Lapidus, Y. Ren, Q. Huang, J. Chen and X. Xing, *Inorg. Chem.*, 2018, **57**, 10918–10924.

43 Z. Song, H. Li, W. Liu, H. Zhang, J. Yan, Y. Tang, J. Huang, H. Zhang and X. Li, *Adv. Mater.*, 2020, **32**, 2001001.

44 F. Shen, Z. Sun, Q. He, J. Sun, R. B. Kaner and Y. Shao, *Mater. Horiz.*, 2021, **8**, 1130–1152.

45 X. Han, Q. Meng, X. Wan, B. Y. Sun, Y. Zhang, B. C. Shen, J. L. Gao, Y. L. Ma, P. J. Zuo, S. F. Lou and G. P. Yin, *Nano Energy*, 2021, **81**, 105635.

46 T. F. Yi, H. M. K. Sari, X. Z. Li, F. F. Wang, Y. R. Zhu, J. H. Hu, J. J. Zhang and X. F. Li, *Nano Energy*, 2021, **85**, 105955.

47 J.-T. Han and J. B. Goodenough, *Chem. Mater.*, 2011, **23**, 3404–3407.

48 Y. Yang, H. Zhu, J. Xiao, H. Geng, Y. Zhang, J. Zhao, G. Li, X. L. Wang, C. C. Li and Q. Liu, *Adv. Mater.*, 2020, **32**, 1905295.

49 A. Kushima, X. Qian, P. Zhao, S. Zhang and J. Li, *Nano Lett.*, 2015, **15**, 1302–1308.

50 H. Zhu, Y. Huang, J. Ren, B. Zhang, Y. Ke, A. K. Jen, Q. Zhang, X. L. Wang and Q. Liu, *Adv. Sci.*, 2021, **8**, 2003534.

51 Q. Li, H. Zhu, L. Zheng, L. Fan, N. Wang, Y. Rong, Y. Ren, J. Chen, J. Deng and X. Xing, *Nano Lett.*, 2017, **17**, 7892–7896.

52 N. H. Bashian, S. Zhou, M. Zuba, A. M. Ganose, J. W. Stiles, A. Ee, D. S. Ashby, D. O. Scanlon, L. F. J. Piper, B. Dunn and B. C. Melot, *ACS Energy Lett.*, 2018, **3**, 2513–2519.

53 A. Wadsley, S. Andersson, J. Dunitz and J. Ibers, *Perspectives in Structural Chemistry*, Wiley, New York, 1970, vol. 3, pp. 1–58.

Electronic Supplementary Material (ESI) for Energy & Environmental Science.

Supplementary for

Pre-zeolite framework super-MIEC anodes for high-rate lithium-ion batteries

Shitong Wang, Lijiang Zhao, Yanhao Dong, He Zhu, Yang Yang, Haowei Xu, Baoming Wang, Yakun Yuan, Yang Ren, Xiaojing Huang, Wei Quan, Yutong Li, Yimeng Huang, Charles M. Settens, Qi He, Yongwen Sun, Hua Wang, Zunqiu Xiao, Wenjun Liu, Xianghui Xiao, Riqiang Fu, Qiang Li, Yong S. Chu, Zhongtai Zhang, Qi Liu, Andrew M. Minor, Junying Zhang, Zilong Tang, and Ju Li

Correspondence to: dongyanhao@tsinghua.edu.cn (Y. Dong), zjy@buaa.edu.cn (J. Zhang), tzl@tsinghua.edu.cn (Z. Tang), liju@mit.edu (J. Li).

This PDF file includes:

Methods
Supplementary Figs. S1 to S24
Supplementary Tables S1 to S7
Supplementary References 1 to 83

Methods

Materials synthesis

H-Nb_2O_5 was synthesized by heat-treating Nb_2O_5 (99.99% purity) at 1125 °C for 5 h. NPO was synthesized by mixing Nb_2O_5 (99.99% purity) and P (99.8% purity) with the Nb: P molar ratio of 9:1.1 (10% access P was added to compensate for P loss during heat treatment), followed by heat treatment at 1100 °C for 20 h. TNO was synthesized by mixing Nb_2O_5 (99.99% purity) and TiO_2 (99.8% purity) with the Nb: Ti molar ratio of 2:1, followed by heat treatment at 1125 °C for 5 h. NWO was synthesized by mixing Nb_2O_5 (99.99 % purity) and WO_3 (99.99% purity) with the Nb: W molar ratio of 9:8, followed by high-temperature treatment at 1100 °C for 20 h. NWT944 and NWT926 were synthesized by mixing NbC (99.99 % purity) and TiO_2 (99.8 % purity) and WO_3 (99.99% purity) with Nb: W: Ti molar ratio of 9:4:4 and 9:2:6, respectively, followed by high-temperature treatment at 1100 °C for 10 h. To synthesize H-Nb_2O_5-B, Nb_2O_5 (99.99% purity) powders were first cold-pressed into a pellet under 50 MPa and heat-treated at 1200 °C for 3 h. The heat-treated pellet was ground, mixed with ethanol, and ball-milled at 350 rpm for 6 h. After ball milling, the slurry was dried in a vacuum oven at 60 °C for 6 h, and then sieved by 150 and 600 meshes to obtain H-Nb_2O_5-B. A heating rate of 2 °C min^{-1} and furnace cooling was used in all heat treatment processes.

Material characterizations

In-situ X-ray diffraction for CTE measurements: X-ray diffraction (XRD, Burke D8 ADVANCE; Cu K_α radiation with wavelength λ=1.5418 Å) with a temperature control stage was used to characterize the phase and the temperature-dependent structural information. Temperature-dependent XRD measurements for H-Nb_2O_5, NPO, NTO, NWO, NWT926, $Li_{0.2}Nb_2O_5$, and $Li_{1.6}Nb_2O_5$ were firstly conducted at 100 K, and then at higher temperatures from 150 K to 650 K with 50 K temperature interval, a ramping rate of 2 K min^{-1}, and 10 min constant-temperature rest before measurement at each temperature. Profile fittings for H-Nb_2O_5, NPO, NTO, NWO, $Li_{0.2}Nb_2O_5$, and $Li_{1.6}Nb_2O_5$ were conducted on the PANalytical X'Pert HighScore Plus[1] at the Center for Materials Science and Engineering, MIT. For NWT926 material, the temperature-dependent lattice parameters were extracted by using Fullprof software[2]. Rietveld refinement was carried out based on the monoclinic $C2/c$ unit cell.

Synchrotron high energy XRD and PDF measurements: The high energy XRD and PDF data were collected using the 11-ID-C beamline at the Advanced Photon Source (APS) of Argonne National Laboratory (ANL), with the X-ray wavelength of 0.1173 Å. Si (113) single crystal was used as a monochromator for an X-ray beam at 105.7 keV. In a typical data collection, the NWT926 powder sample (for high energy XRD measurement), H-Nb_2O_5, and $Li_{0.1}Nb_2O_5$ powder samples (for PDF measurements) were loaded into a 3 mm capillary with a data acquisition time of 20 minutes. The background was extracted from the same empty capillary. A two-dimensional Perkin-Elmer detector was used to record the scattering patterns in transmission mode. Fit 2D software was applied to calibrate the scattering patterns with the CeO_2 standard sample and integrate the 2D patterns into 1D profiles[3]. The $G(r)$ function was computed by Fourier transform of reduced structural function ($F(Q)$, up to 17.6 $Å^{-1}$) with PDFgetX2 software[4]. The Rietveld method was used to determine the crystal structure of NWT926 using Fullprof software[2]. A monoclinic $C2/c$ unit cell was built to describe the XRD pattern. The pseudo-Voigt peak-shape function was used to fit the full width at half maximum (FWHM) with fitting parameters U, V, W, and Gaussian/Lorentz ratio. Due to the structural complexity of NWT926, not all the atomic information can be extracted. The atomic coordination values in Table S2, ESI† were inherited from the pristine NWO structure with undistorted octahedra, while the occupancies were calculated based on the stoichiometric ratio. The current structural model can describe the XRD pattern reasonably well. The resolution of the collected XRD data is insufficient to provide complete atomic information, and single-crystal diffraction experiments need to be carried out to determine the exact structure of NWT926 in the future studies to fully resolve the structure.

Morphology and structural characterizations: A scanning electron microscope (SEM, MERLIN VP Compact) was used to characterize the morphology. A Ga-focused ion beam (Ga-FIB) system (FEI Helios G4) was used to lift out a thin TEM lamella from H-Nb_2O_5 particles. The H-Nb_2O_5 particles were protected by Pt deposition before lift-out. During the thinning process, the energy of the ion beam was reduced from 30 to 16, 8, 5, 2, 1 keV step by step. TEAM-1, a double aberration-corrected TEM operating at 300 kV at the national center for electron microscopy

(NCEM) in the Lawrence Berkeley National Laboratory, was used to collect atomic-resolution STEM-HAADF images. Image pairs with orthogonal scan directions were collected and a MATLAB code developed by Ophus et al.[5] was used to correct the nonlinear scan distortion. The 4D-STEM experiments were performed on an FEI Titan operating at 300 keV. A 10 μm condenser C2 aperture and a convergence angle of 0.12 mrad were chosen to form a nanosized electron beam with a full width half maximum (FWHM) of about 12 nm. The scan step size was 10 nm. The camera length was 480 mm. The py4DSTEM package[6] was used for the analysis of 4D-STEM data.

Method of stacking fault mapping: Conventional STEM-HAADF images cannot depict the location of SFs accurately due to the co-existence of multiple structural information. To better map the SFs/twins in the sample, a new method is developed. For regions with stacking faults (SFs), diffuse streaks between Bragg peaks will show up in the nanobeam electron diffraction (NBED) patterns. Because the streaks due to SFs tend to make the Bragg peaks more elliptical, the averaged aspect ratio (a/b, where a and b are the length of the long axis and length of the short axis, respectively) of Bragg peaks in an NBED pattern can be correlated to the relative density of SFs. When there are more SFs, a/b is smaller. While there are no SFs, a/b is close to 1. To calculate a/b, windows of 20 pixels by 20 pixels in size are chosen whose center overlaps with each Bragg peak. The standard deviation along the streak direction and perpendicular to the streak direction is calculated as a and b, respectively. py4DSTEM package[6] is used to find the location of each Bragg peak.

Methods of displacement analysis: The cross-sectional $Li_{0.1}Nb_2O_5$ TEM specimen was prepared using a Thermo Fisher Helios 600 focused ion beam (FIB)/SEM microscope. The specimen was first coated with 10 nm carbon using Denton DV502A Evaporator to minimize the beam damage and charging effects. Additive protective layers were deposited by combining e-beam and ion-beam deposition in the FIB instrument, including an e-beam-deposited 100 nm Pt layer and an ion-beam-deposited 1 μm carbon layer. The sample was thinned step by step by lowering ion voltages from 30 kV to 2 kV and currents from 0.92 nA to 89 pA. The surface damage caused by FIB is further removed by argon ion milling using a Fischione 1051 TEM Mill at room temperature with a voltage of 100 V and angle of 7°. The high-resolution HAADF images are taken in a Thermo Fisher Themis Z-STEM at MIT with an acceleration voltage of 200 kV. The potential atom positions were obtained by identifying the local maxima of the HAADF image. After manual correction of the misidentified positions, a Gaussian function was used to fit a 5×5 pixels area around each local maxima, which generated a list of 2D coordinates of the atoms from the experimental image. Then, a unit cell was selected by identifying and averaging the smallest repeating unit of the atomic structure. A reference lattice was generated by periodically repeating the averaged unit cell in two in-plane directions of the image. Finally, the displacement vectors were calculated by comparing the experimental atomic coordinates with the reference lattice.

Characterizations of H_2O adsorption/desorption: Thermogravimetric analysis (TGA) was carried out using NETZSCH-STA 449 F3 with a heating rate of 10 °C min^{-1} under an air atmosphere. The powder samples were suspended in deionized H_2O for 10 mins, then collected and dried at 60 °C for 5 h.

Characterizations of chemical compositions and surface areas: Because of the low volatility of Nb, Ti and W elements, the ratios of transition metal (TM) were determined by the ratios of the raw materials, and the ratio of TM/O was determined by balancing the valance (as the synthesis was conducted at oxidation environment, we assumed +5 for Nb, +6 for W, and +4 for Ti). Inductively coupled plasma mass spectroscopy (ICP-MS, iCP QC, Thermo Fisher Scientific) measurements were also conducted to confirm the ratios of TM. The specific surface area was measured by Autosorb-iQ2-MP (Quanta Chrome) and calculated following the Brunauer-Emmett-Teller (BET) method.

Electrochemical measurements

Preparation of half cells: To prepare the composite working electrodes, active materials, conductive carbon, and binder were mixed with a specific weight ratio to form a homogeneous slurry, spread on commercial Al foils (for H-Nb_2O_5, H-Nb_2O_5-B, NPO, NTO, NWO, NWT944, NWT926, $Li_4Ti_5O_{12}$, $LiCoO_2$, $LiNi_{0.33}Co_{0.33}Mn_{0.33}O_2$, $LiNi_{0.6}Co_{0.2}Mn_{0.2}O_2$, $LiNi_{0.5}Mn_{1.5}O_4$, and $LiFePO_4$) or Cu foils (for meso-carbon microbeads), and dried at 110 °C in vacuum for 12 h. $Li_4Ti_5O_{12}$, $LiCoO_2$, $LiNi_{0.33}Co_{0.33}Mn_{0.33}O_2$, $LiNi_{0.6}Co_{0.2}Mn_{0.2}O_2$, $LiNi_{0.5}Mn_{1.5}O_4$, $LiFePO_4$, and meso-carbon microbeads were obtained from commercial vendors, while others were home-synthesized. The slurries of H-Nb_2O_5, H-Nb_2O_5-B, NPO, NTO, NWO, NWT944, and NWT926 were prepared using water as the solvent, and sodium carboxymethyl cellulose (CMC) and polymerized styrene-butadiene rubber (SBR) with a weight ratio of 1:1 as the binder. The slurries of $Li_4Ti_5O_{12}$, $LiCoO_2$, and $LiNi_{0.33}Co_{0.33}Mn_{0.33}O_2$, $LiNi_{0.6}Co_{0.2}Mn_{0.2}O_2$, $LiNi_{0.5}Mn_{1.5}O_4$, and $LiFePO_4$ were prepared using N-methyl-2-pyrrolidone (NMP) as the solvent, and polyvinylidene fluoride (PVDF) as the binder. Mass loadings for the electrodes in half cells were controlled between 1.0~3.0 mg cm^{-2}. 1 M $LiPF_6$ dissolved in ethylene carbonate (EC), dimethyl carbonate (DMC), and ethyl methyl carbonate (EMC) in a 1:1:1 volume ratio, and 1 M $LiClO_4$ dissolved in propylene carbonate (PC) was used as the electrolyte. The electrolyte volume in this experimental section is excess (~50 mL Ah^{-1}). The Li metal used in half cells is 0.45 mm thick with the diameter of 18 mm. Microporous polypropylene films (Celgard 2500) were used as the separator. Cell assembly (CR2032 type) was carried out in an Ar glove box with oxygen and water contents below 1.0 ppm and 0.5 ppm, respectively. Charge/discharge tests and galvanostatic intermittent titration technique (GITT) were conducted at varied current densities using a LAND battery testing system (CT-2001A). Detailed information on electrode compositions, half-cell cycling window, and GITT measurements was listed in Table S7, ESI†.

Preparation of lithiated samples for characterizations: H-Nb_2O_5 electrode (without the addition of binder and conductive carbon) was prepared by cold pressing under 20 MPa. Li||H-Nb_2O_5 half-cells were assembled by using Li metal as the counter and reference electrode and 1.0 M $LiPF_6$ in EC: DMC: EMC as the electrolyte. The cells were discharged at 50 mA g^{-1} to the set potentials: 2.0 V for $Li_{0.1}Nb_2O_5$, 1.8 V for $Li_{0.2}Nb_2O_5$, 1.3 V for $Li_{1.6}Nb_2O_5$, respectively. Lithiated materials were obtained from disassembled cells, followed by washing (by DMC solvent) and drying repeated three times.

Electronic conductivity measurements: Testing cells for electronic conductivity measurements were assembled by sandwiching the lithiated materials between stainless steels as the two blocking electrodes (blocking to Li^+), and cold-pressing under 20 MPa. The electronic resistance (R) for Nb_2O_5 and $Li_{0.1}Nb_2O_5$ was measured by a direct current (DC) method. 50 mV DC voltage was applied to the cell, and the steady-state current was recorded after ~1 h where the current changed less than 1 μA g^{-1} per minute. The electronic conductivity (σ_e) was calculated by the geometry of the pressed materials.

Preparation of full cells: H-Nb_2O_5 vs. $LiNi_{0.5}Mn_{1.5}O_4$ and H-Nb_2O_5 vs. $LiFePO_4$ coin-cell type full cells (CR2032 type) were assembled and tested. H-Nb_2O_5 vs. $LiNi_{0.6}Co_{0.2}Mn_{0.2}O_2$ pouch-type full cells and H-Nb_2O_5-B vs. $LiCoO_2$ pouch-type full cells were also assembled and tested. Mass loading for the anodes in full cells was controlled between 5.0~16.0 mg cm^{-2}. Mass loading for the cathodes in full cells was controlled between 7.0~14.0 mg cm^{-2} to match with the optimized negative to positive capacity (N/P) ratio. More details are listed in Table S7, ESI†.

Model and simulation

First-principles calculations: Spin-polarized first-principles calculations were conducted on Vienna ab initio simulation package (VASP) using projector augmented-wave (PAW) method with Perdew-Burke-Ernzerhof (PBE) generalized gradient approximation (GGA)[7-10]. We used PAW potentials with 1 valence electron for Li, 13 valence electrons for Nb, 6 valence electrons for O, and plane-wave cutoff energy of 520 eV. Li storage in H-Nb_2O_5 was simulated by adding 1 Li to the described sites in a 1×3×1 supercell containing 84 Nb and 210 O. Convergence was considered as reached when residue atomic forces were less than 0.05 eV $Å^{-1}$. Li^+ migration was simulated in the same supercell, using the climbing image nudged elastic band (NEB) method[11]. The convergence of NEB calculations was set to be reached when the residual atomic forces were less than 0.1 eV $Å^{-1}$. The Brillouin zone was sampled using the Monhorst-Pack scheme with a 1×1×1 k-point mesh. Atomic structures were visualized and plotted using VESTA[12].

RMC simulations: Initial structural model for RMC simulations was generated using a 3×5×13 supercell of the perfect H-Nb_2O_5 unit cell, containing 3780 Nb and 9450 O in total. For $Li_{0.1}Nb_2O_5$, Li atoms were not included in RMC simulations because of the weak diffraction signal of Li. RMC simulations were conducted using the software RMCprofile[13]. The minimum distance windows of Nb…O, Nb…Nb, and O…O atom pairs were set as 1.9 Å, 2.8 Å, and 1.3 Å, respectively, while their maximum distance windows were 3.5 Å, 4.0 Å, and 2.5 Å, respectively.

Supplementary Figures

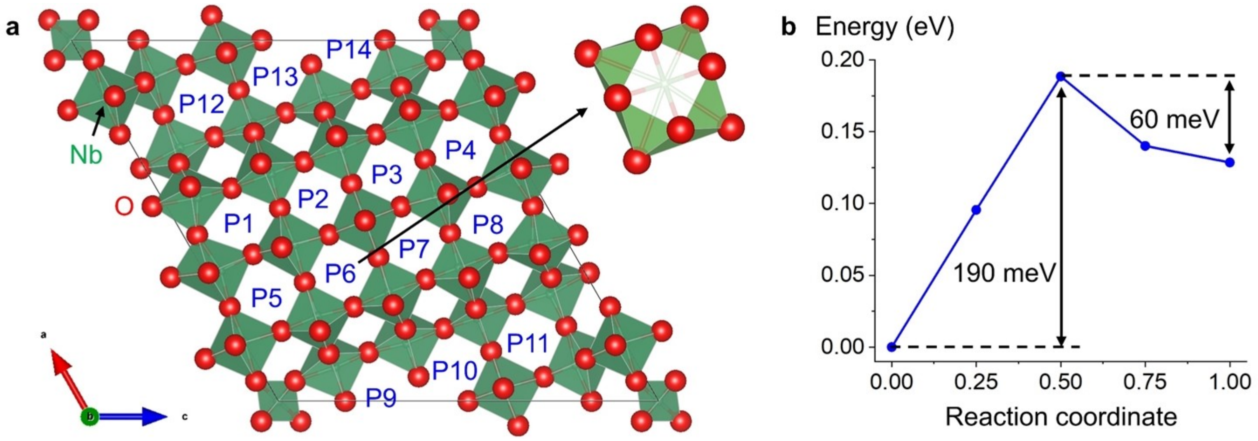

Fig. S1 (a) Atomic structure of block structure oxide H-Nb_2O_5. Tunnels marked as P1 to P14 within one unit cell. (b) Calculated migration barrier for Li^+ between two neighboring square-planar sites from one on the sidewall to the one in the *a*-*c* plane within the P6 tunnel.

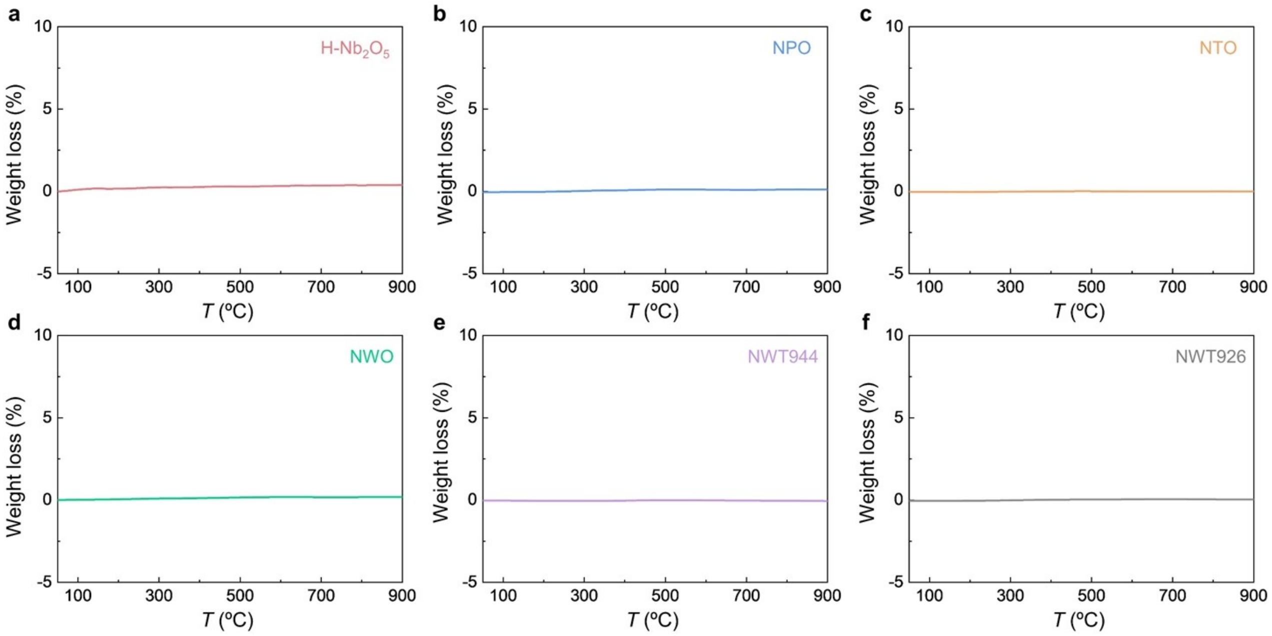

Fig. S2 H_2O adsorption/desorption study of (a) H-Nb_2O_5, (b) NPO, (c) NTO, (d) NWO, (e) NWT944, and (f) NWT926 by thermogravimetric analysis.

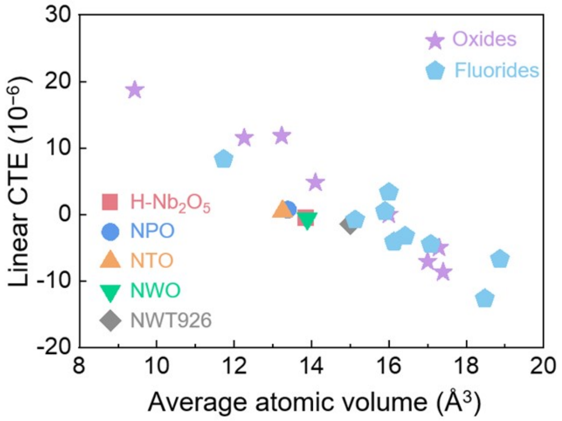

Fig. S3 The correlation between thermal expansion and the average atomic volume for H-Nb$_2$O$_5$, NPO, NTO, NWO, NWT926, and the common oxides and fluorides reported in reference[14].

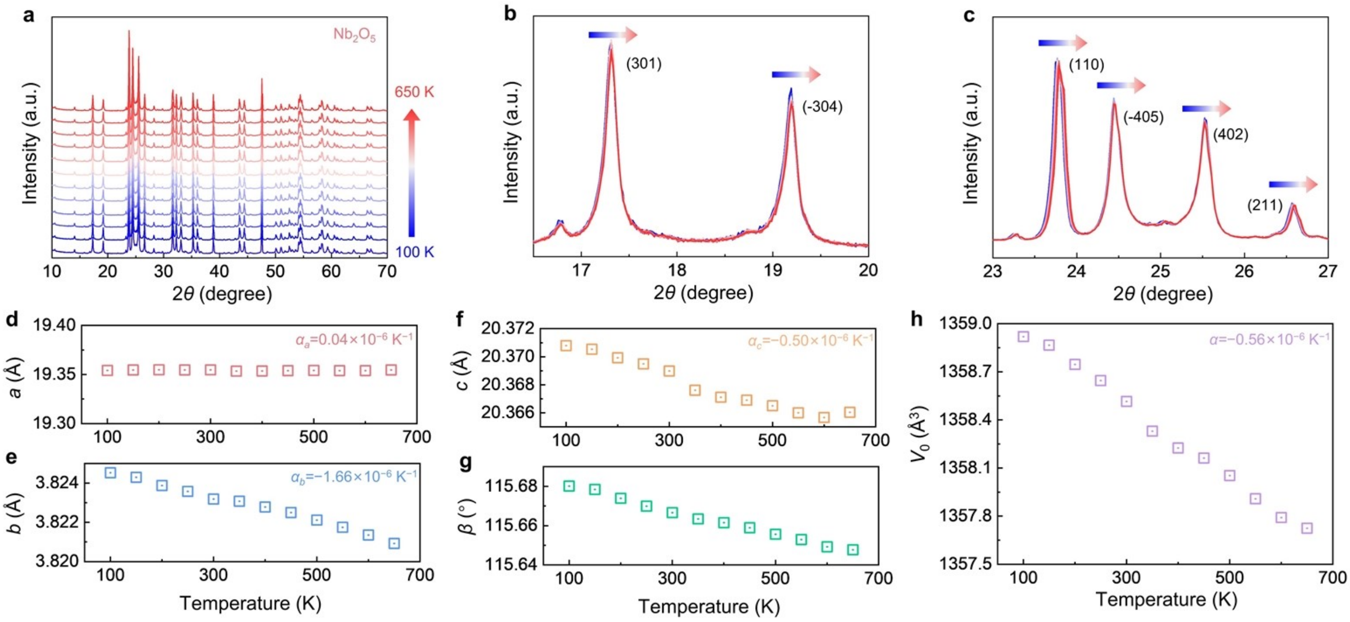

Fig. S4 (a~c) XRD analysis of H-Nb$_2$O$_5$ at 100 K, 150 K, 200 K, 250 K, 300 K, 350 K, 400 K, 450 K, 500 K, 550 K, 600 K, and 650 K. (d~h) Primary-cell parameters as a function of temperature T, together with the calculated coefficient of linear thermal expansion.

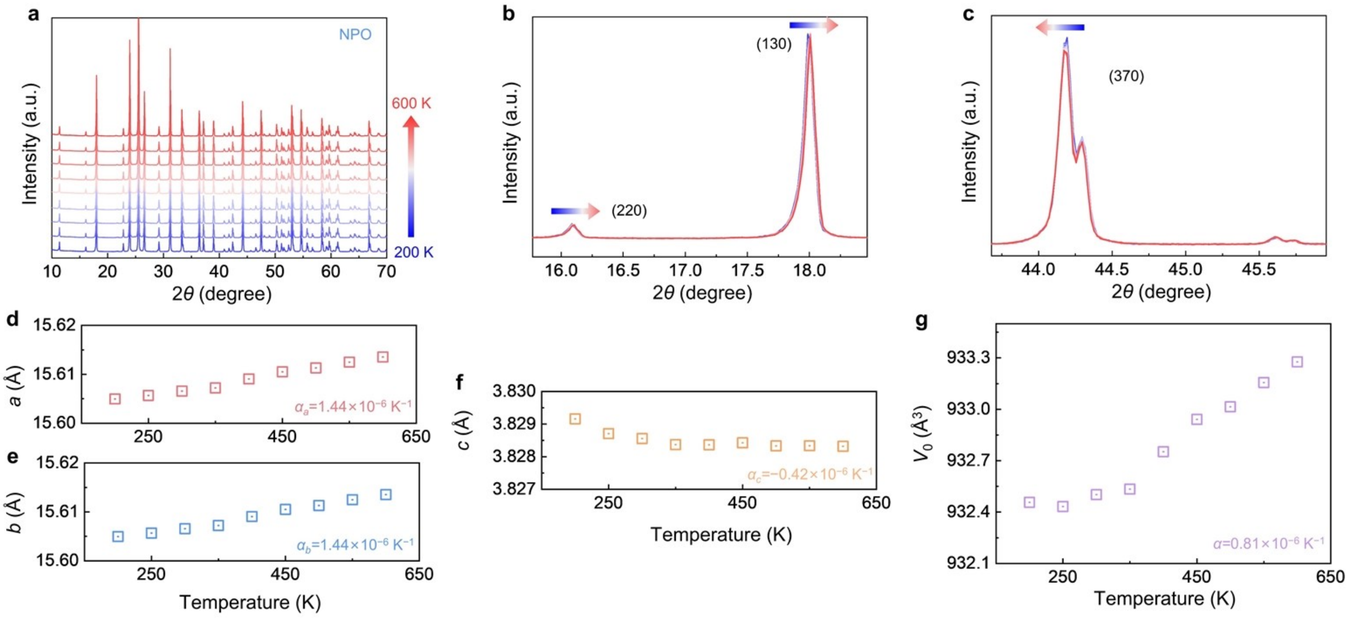

Fig. S5 (a~c) XRD analysis of NPO at 200 K, 250 K, 300 K, 350 K, 400 K, 450 K, 500 K, 550 K, and 600 K. (d~g) Primary-cell parameters as a function of temperature *T*, together with the calculated coefficient of linear thermal expansion.

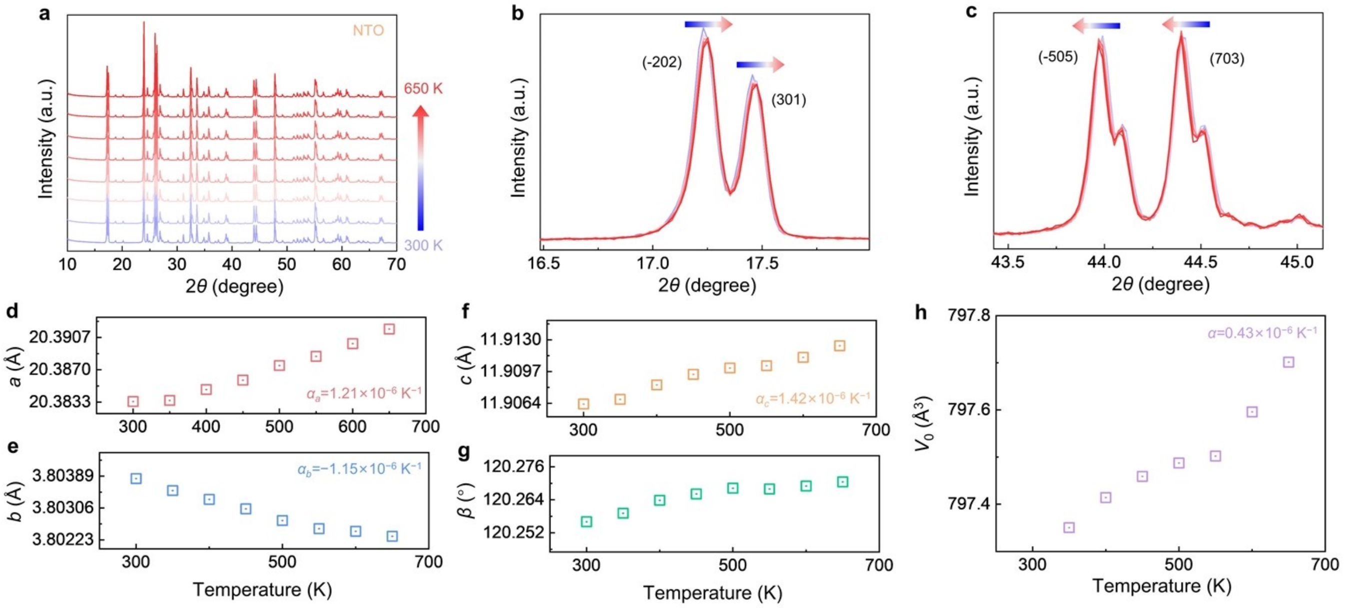

Fig. S6 (a~c) XRD analysis of NTO at 300 K, 350 K, 400 K, 450 K, 500 K, 550 K, 600 K, and 650 K. (d~h) Primary-cell parameters as a function of temperature *T*, together with the calculated coefficient of linear thermal expansion.

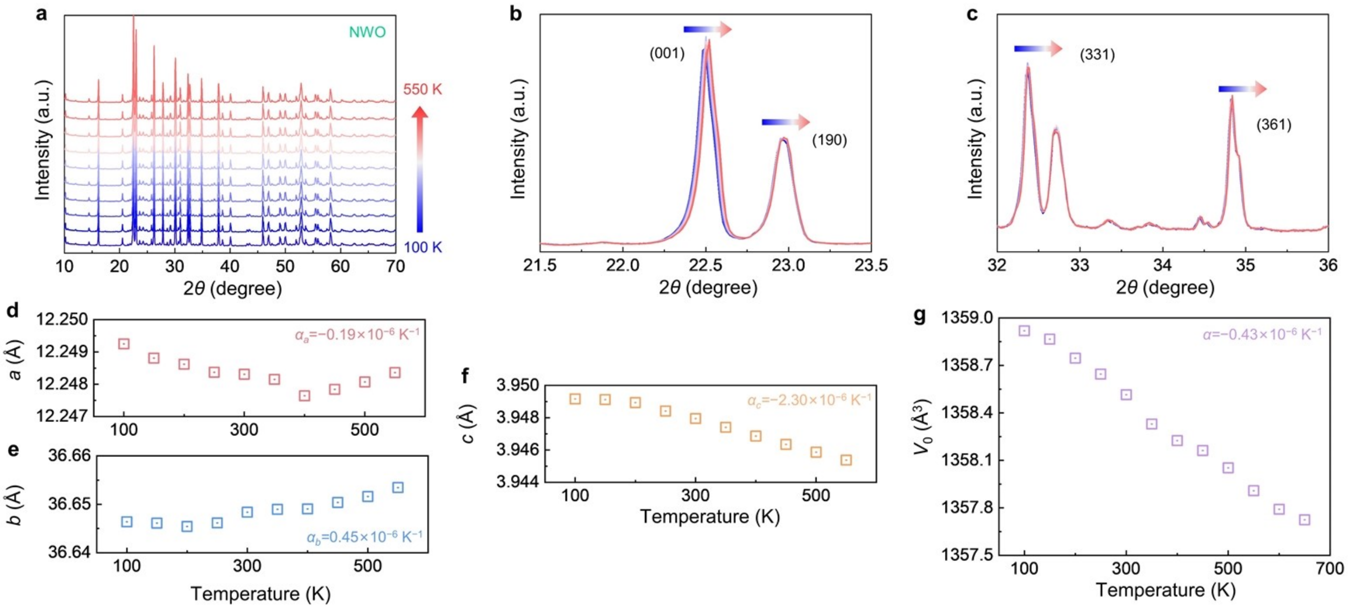

Fig. S7 (a~c) XRD analysis of NWO at 100 K, 150 K, 200 K, 250 K, 300 K, 350 K, 400 K, 450 K, 500 K, and 550 K. (d~g) Primary-cell parameters as a function of temperature *T*, together with the calculated coefficient of linear thermal expansion.

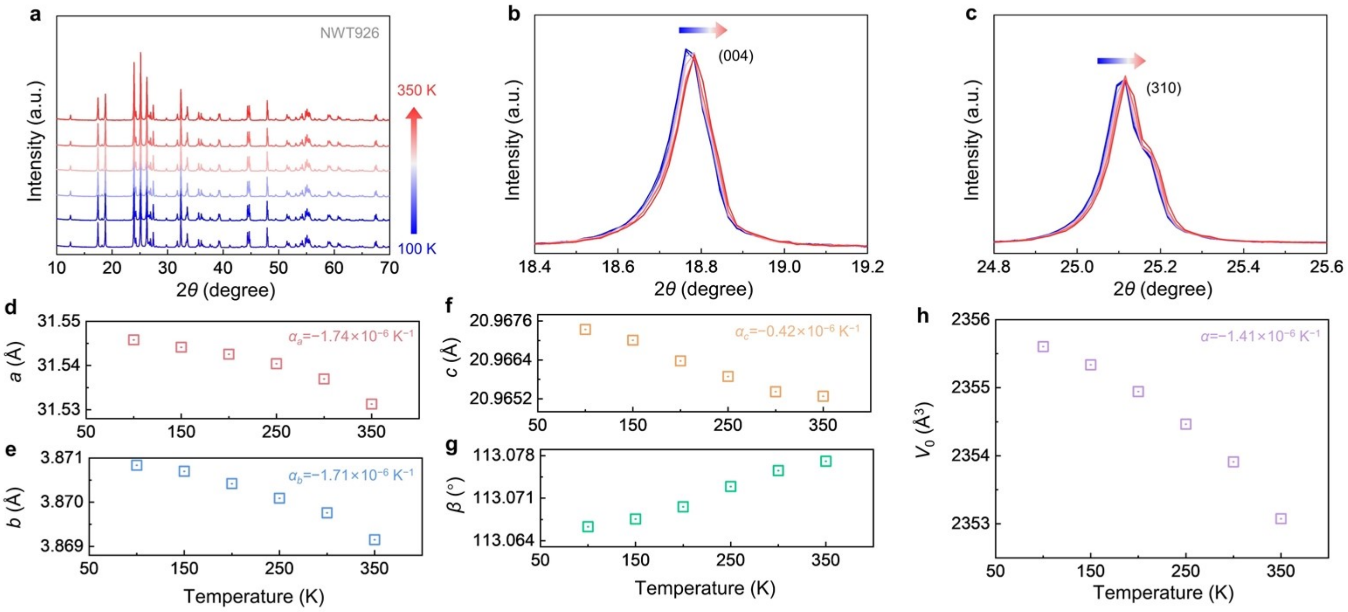

Fig. S8 (a~c) XRD analysis of NWT926 at 100 K, 150 K, 200 K, 250 K, 300 K, and 350 K. (d~h) Primary-cell parameters as a function of temperature *T*, together with the calculated coefficient of linear thermal expansion.

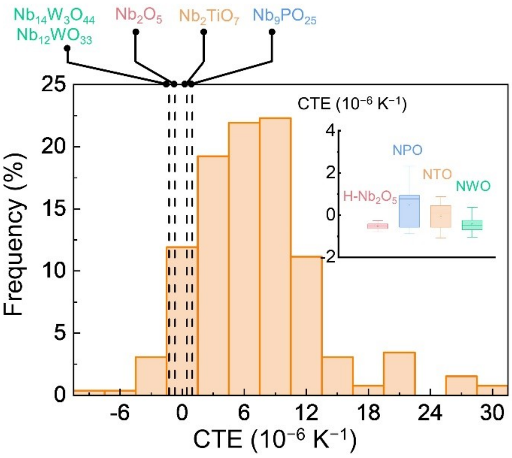

Fig. S9 CTEs of 260 materials in the database of Table S2, ESI†. Inset: measured CTEs for H-Nb_2O_5, NPO, NTO, and NWO.

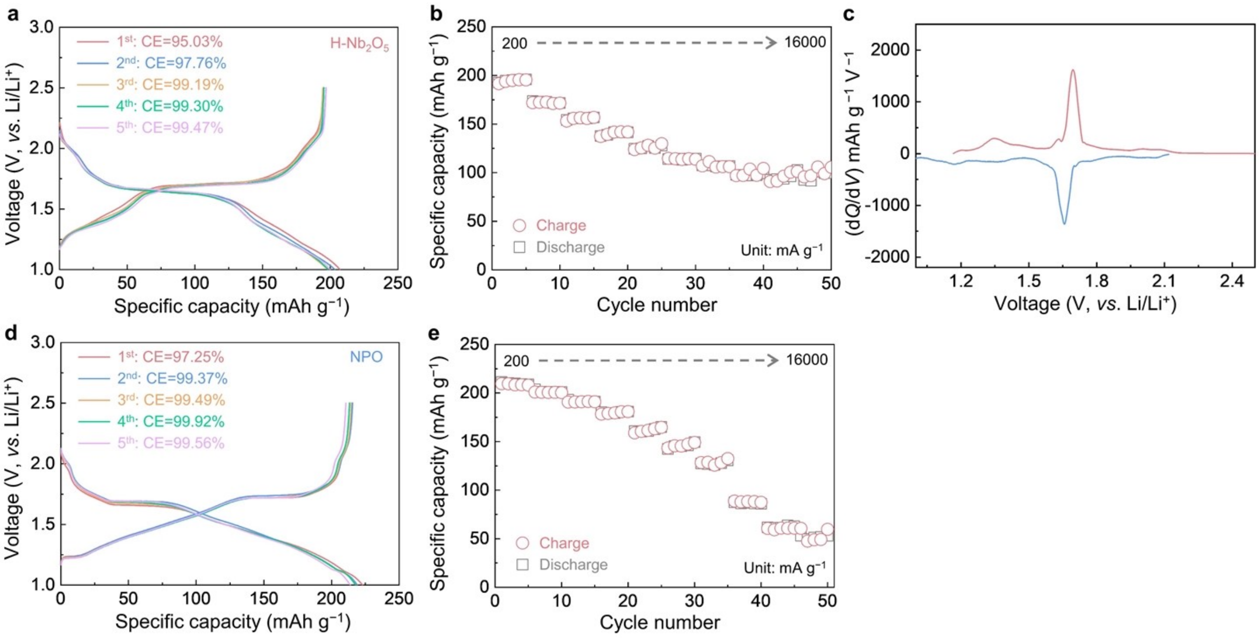

Fig. S10 First five galvanostatic discharge/charge profiles together with Coulombic efficiencies of (a) H-Nb$_2$O$_5$ and (d) NPO at 100 mA g^{-1}. (c) The differential capacity (dQ/dV) plots of the H-Nb$_2$O$_5$. Rate capacities for (b) H-Nb$_2$O$_5$ and (e) NPO at 200, 500, 1,000, 2,000, 4,000, 6,000, 8,000, 10,000, 12,000, and 16,000 mA g^{-1}. From the dQ/dV plots of the H-Nb$_2$O$_5$, there is one pair of sharp reversible peaks at 1.69/1.65 V and two pairs of broad tiny peaks at 1.35/1.17 V and 2.05/2.01 V. The sharp reversible peaks at 1.69/1.65 V together with the broad tiny peaks at 2.05/2.01 V are associated with the redox reactions of Nb^{5+}/Nb^{4+}; while the broad tiny peaks at 1.35/1.17 V are associated with the redox reactions of Nb^{4+}/Nb^{3+}[15]. For the Li storage mechanism, the sharp-peak regions around 1.69/1.65 V are assigned to two-phase reaction; while the broad-peak regions around 1.35/1.17 V and 2.05/2.01 V are assigned to solid-solution reaction[16].

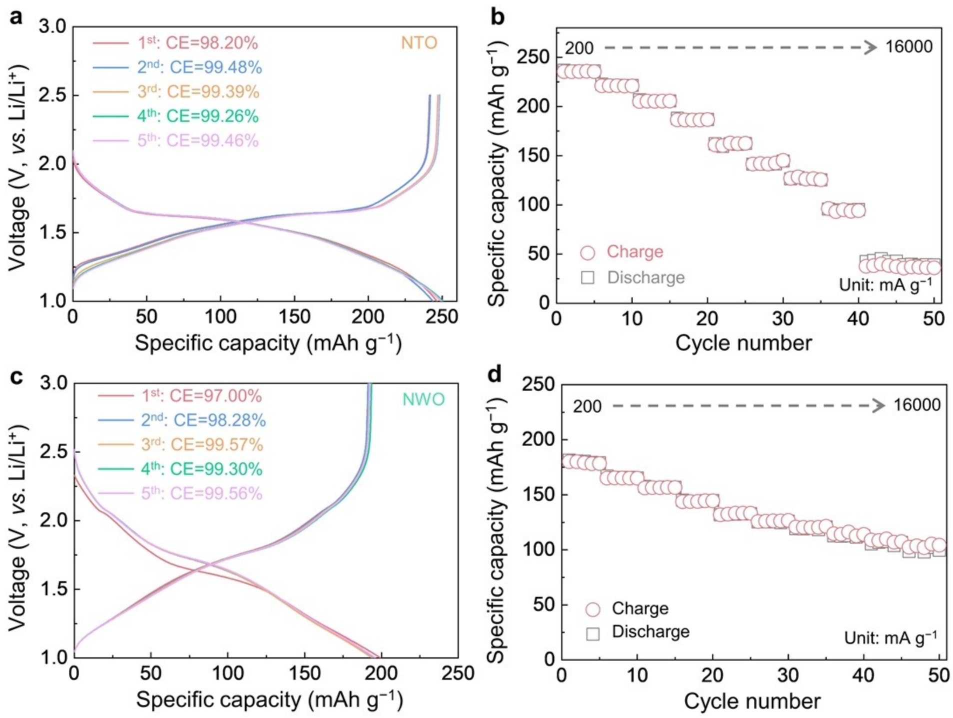

Fig. S11 First five galvanostatic discharge/charge profiles together with Coulombic efficiencies of (a) NTO and (c) NWO at 100 mA g^{-1}. Rate capacities for (b) NTO and (d) NWO at 200, 500, 1,000, 2,000, 4,000, 6,000, 8,000, 10,000, 12,000, and 16,000 mA g^{-1}.

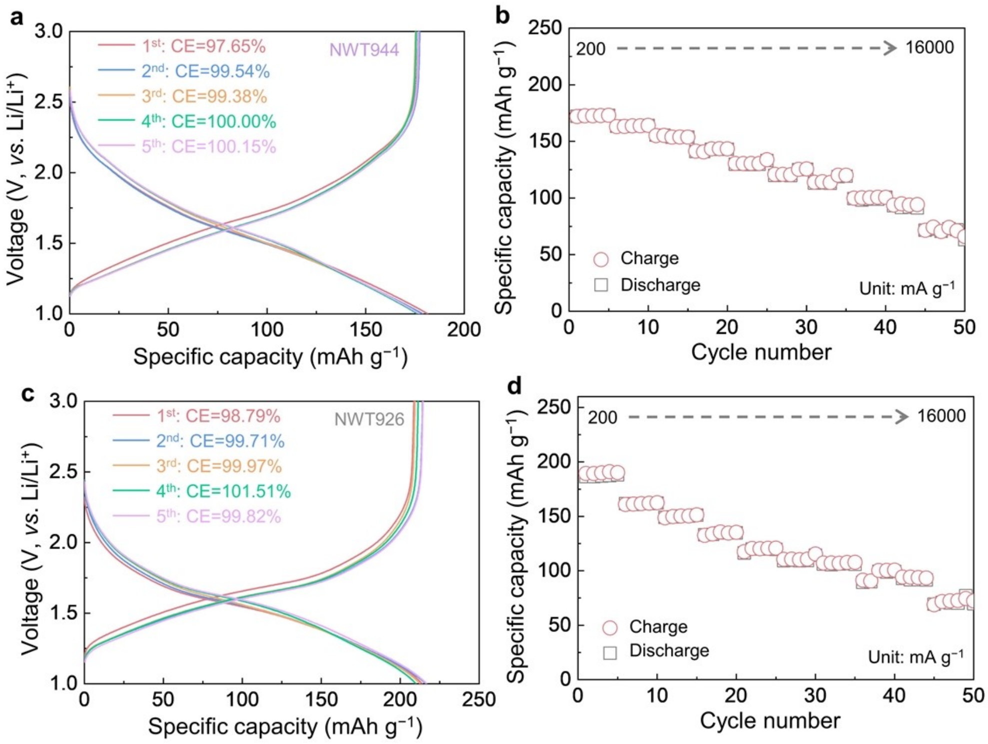

Fig. S12 First five galvanostatic discharge/charge profiles together with Coulombic efficiencies of (a) NWT944 and (c) NWT926 at 100 mA g^{-1}. Rate capacities for (b) NWT944 and (d) NWT926 at 200, 500, 1,000, 2,000, 4,000, 6,000, 8,000, 10,000, 12,000, and 16,000 mA g^{-1}.

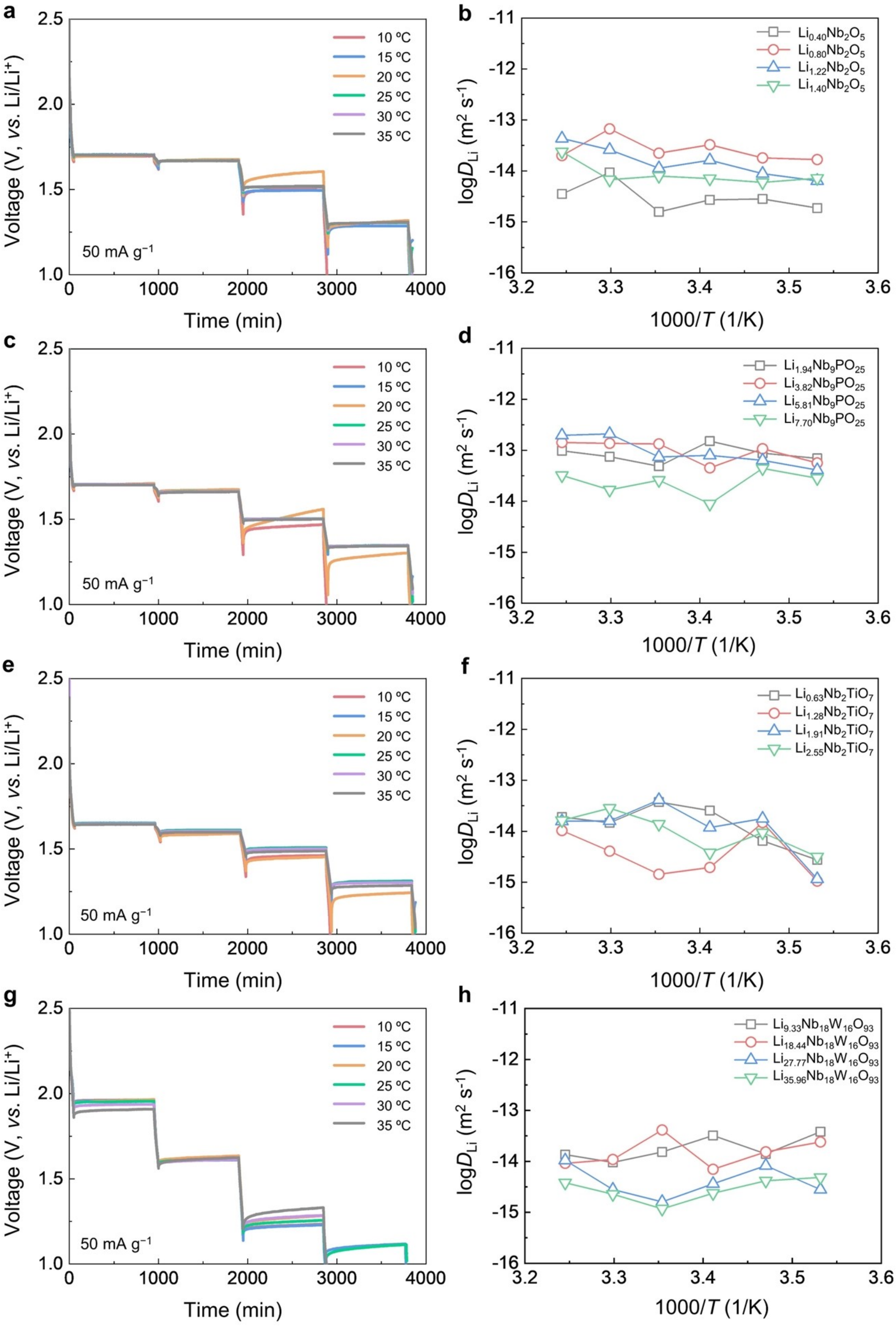

Fig. S13 GITT curves and calculated diffusion coefficients of lithium D_{Li} at 10~35 ºC for (a, b) H-Nb_2O_5, (c, d) NPO, (e, f) NTO, (g, h) NWO by using 1.0 M $LiPF_6$ in EC: DMC: EMC as the electrolyte.

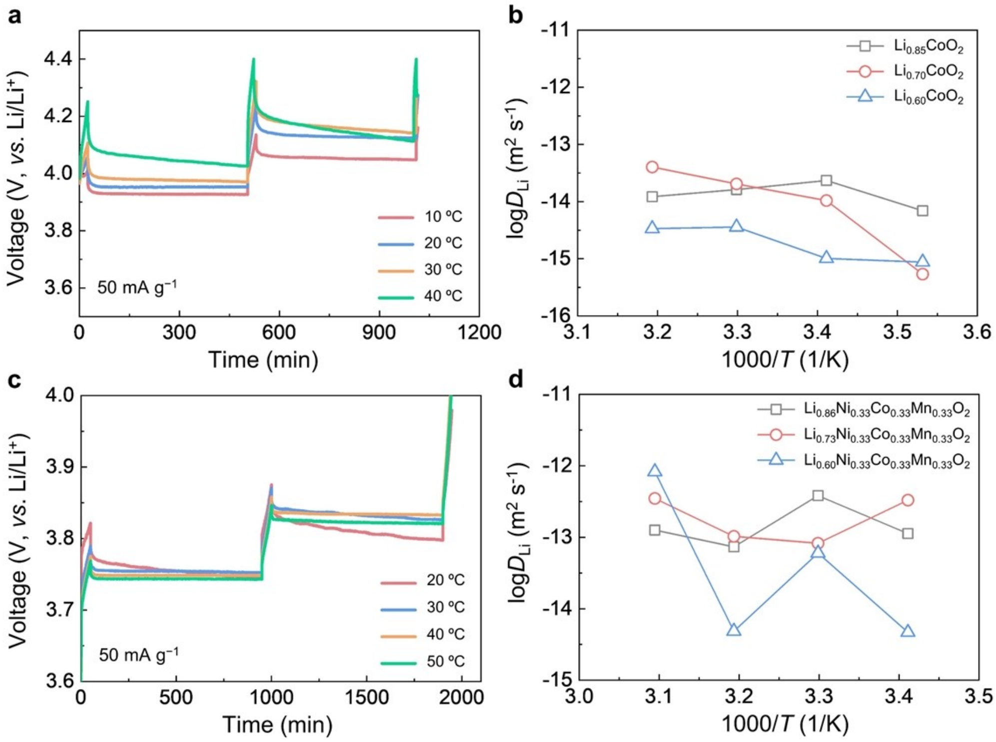

Fig. S14 GITT curves and calculated diffusion coefficients of lithium D_{Li} at (a, b) 10~40 ^{o}C for $LiCoO_2$, and (c, d) 20~50 ^{o}C for $LiNi_{0.33}Co_{0.33}Mn_{0.33}O_2$ by using 1.0 M $LiPF_6$ in EC: DMC: EMC as the electrolyte.

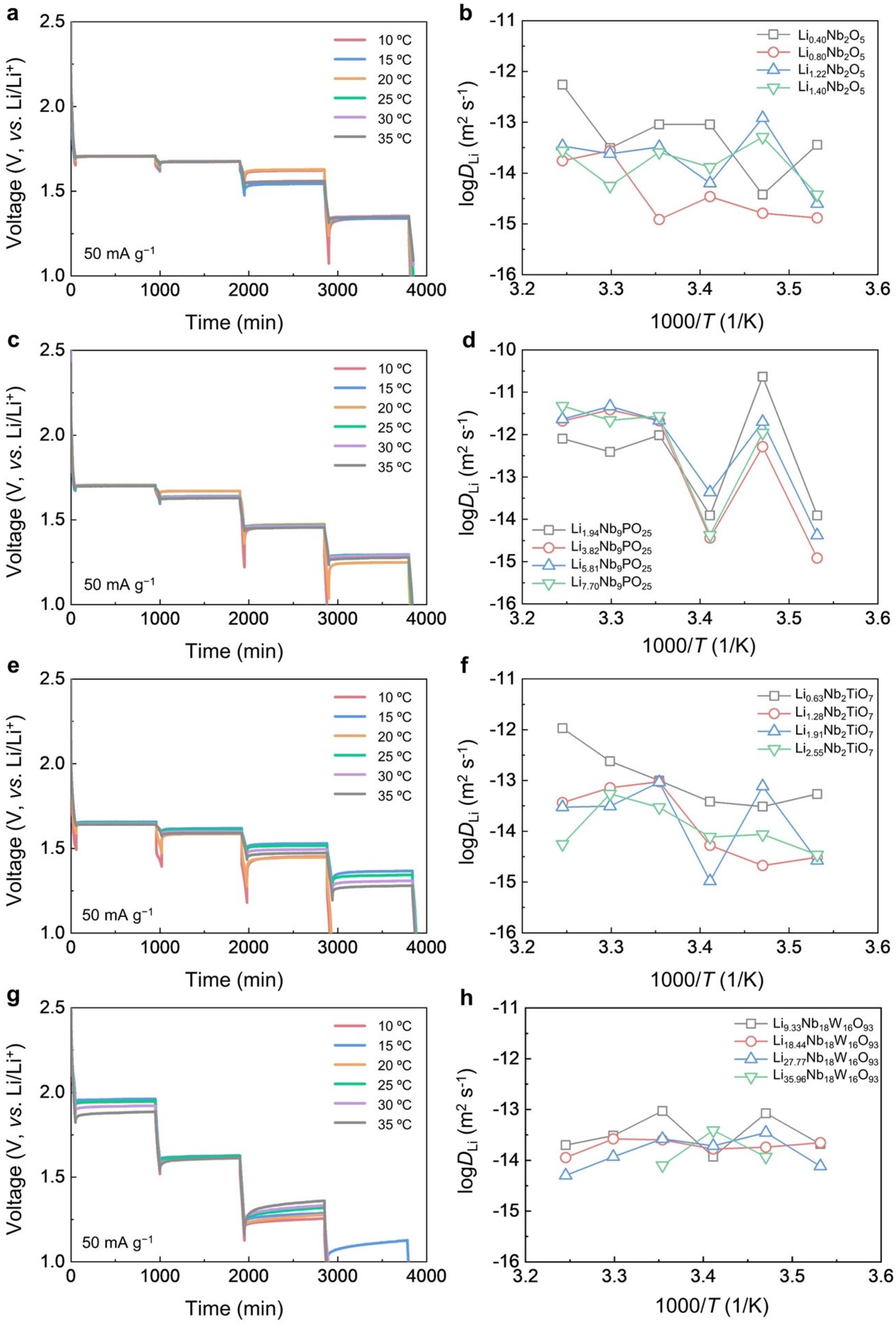

Fig. S15 GITT curves and calculated diffusion coefficients of lithium D_{Li} at 10~35 ^{o}C for (a, b) H-Nb_2O_5, (c, d) NPO, (e, f) NTO, (g, h) NWO by using 1.0 M $LiClO_4$ in PC as the electrolyte.

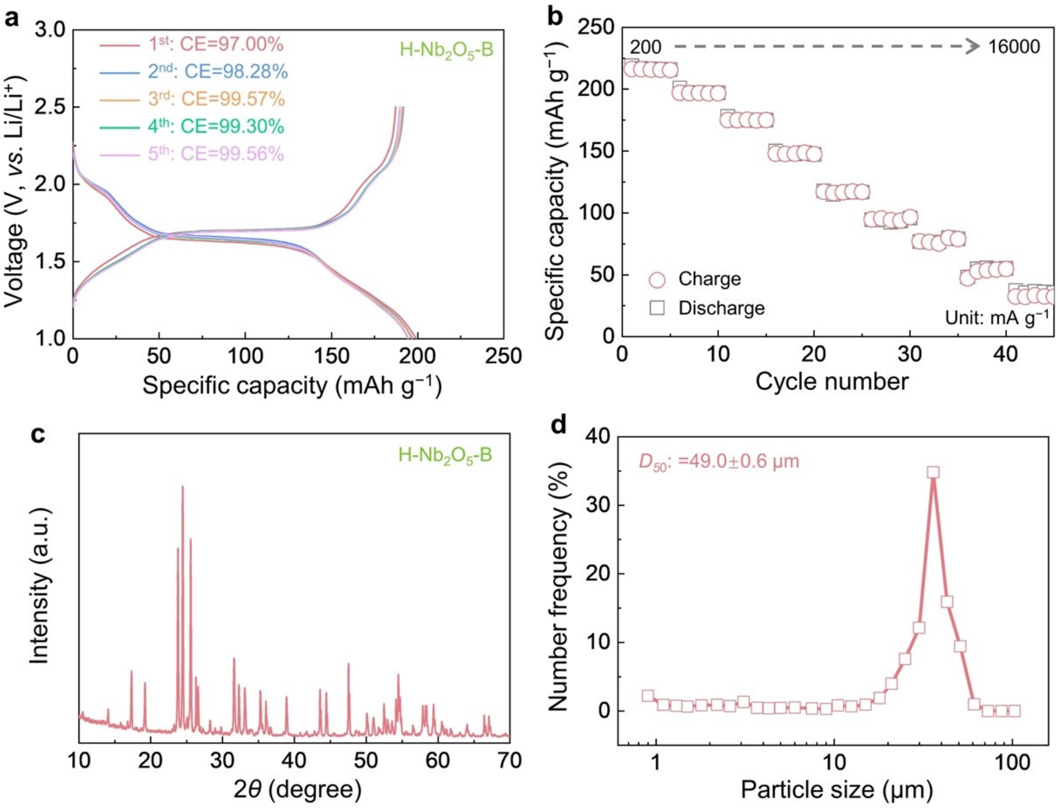

Fig. S16 (a) First five galvanostatic discharge/charge profiles at 100 mA g^{-1} together with Coulombic efficiencies. (b) Rate capacities at 200, 500, 1,000, 2,000, 4,000, 6,000, 8,000, 12,000, and 16,000 mA g^{-1} after 200 cycles at 4,000 mA g^{-1} for electrode activation. (c) XRD pattern and (d) particle distribution analysis for H-Nb_2O_5-B. Note that the high-rate capacity of H-Nb_2O_5-B is not as good as H-Nb_2O_5, because at high current densities (like >6000 mA g^{-1}) H-Nb_2O_5-B has reached the limit of Li^+ transport as well as e^- transport (low content of conductive carbon).

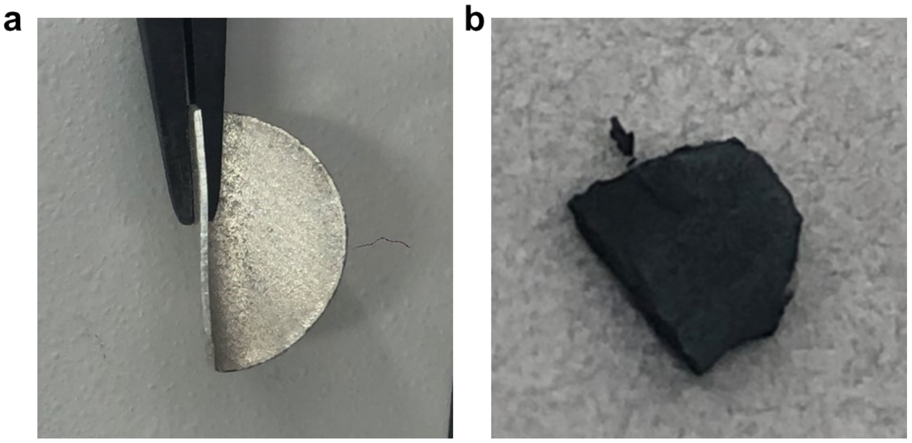

Fig. S17 The photos of Li metal (a) before and (b) after 7300 cycles of the NWT944 half-cell.

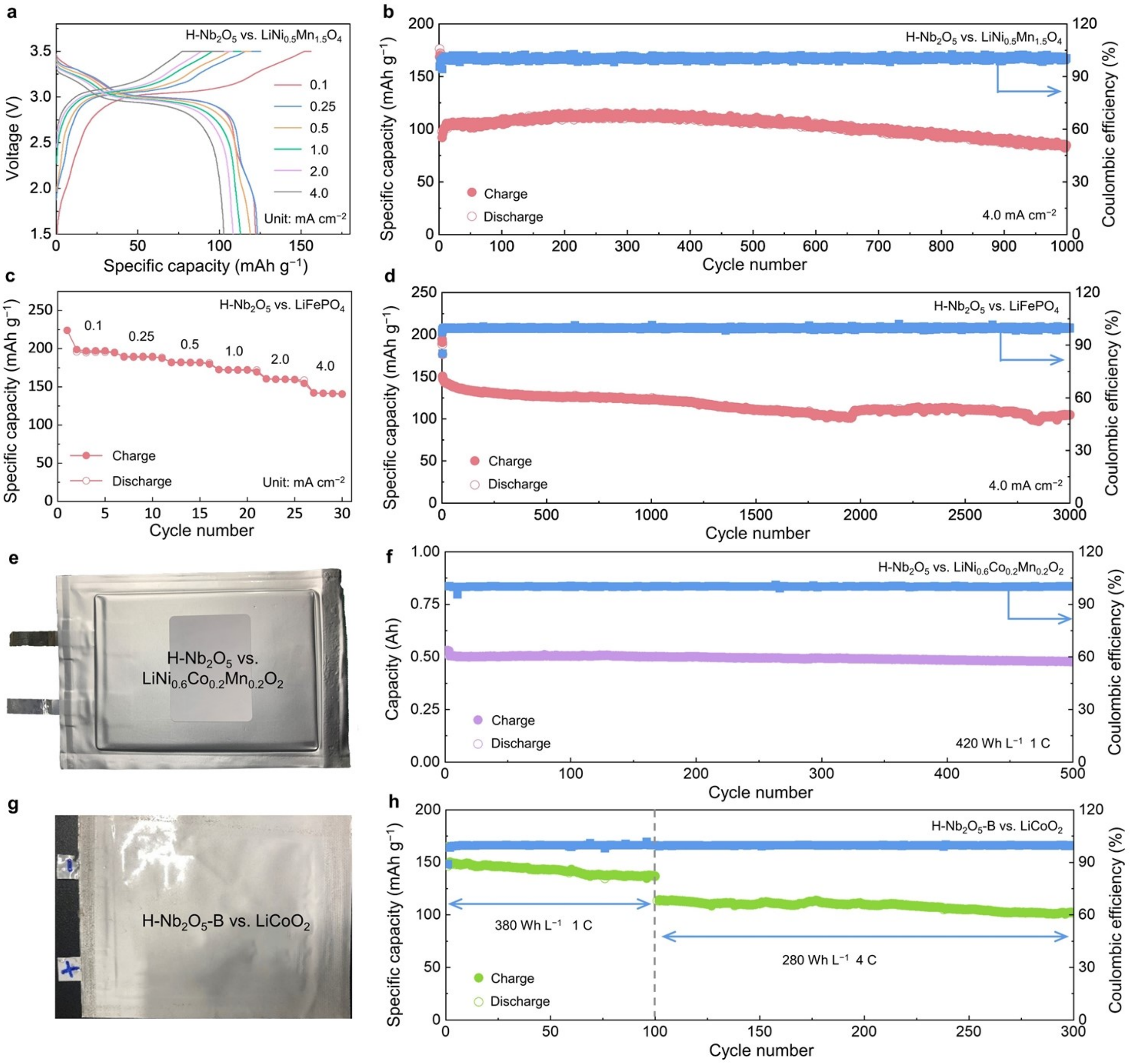

Fig. S18 Full cells performances using H-Nb_2O_5 as the anode. (a) Galvanostatic discharge/charge profiles at 0.1, 0.25, 0.5, 1.0, 2.0, and 4.0 mA cm^{-2} and (b) cycling performances at 4.0 mA cm^{-2} of H-Nb_2O_5 in full cells paired with $LiNi_{0.5}Mn_{1.5}O_4$ cathode. Mass loadings of cathode: 13.6 mg cm^{-2}. Mass loadings of anode: 5.5 mg cm^{-2}. Negative to positive capacity (*N*/*P*) ratio: 0.83. (c) Rate performances and (d) cycling performances at 4.0 mA cm^{-2} of H-Nb_2O_5 in full cells paired with $LiFePO_4$ cathode. Mass loadings of cathode: 7.4 mg cm^{-2}. Mass loadings of anode: 5.2 mg cm^{-2}. *N*/*P* ratio: 1.03. All the specific capacities were calculated by the anodes. (e) Photo and (f) cycling performance of 0.5 Ah H-Nb_2O_5 pouch-type full cells (paired with $LiNi_{0.6}Co_{0.2}Mn_{0.2}O_2$ cathode) at 1 C. Mass loadings of cathode: 8.9 mg cm^{-2}. Mass loadings of anode: 9.0 mg cm^{-2}. *N*/*P* ratio: 1.0. (g) Photo and (h) cycling performance of H-Nb_2O_5-B pouch-type full cells (paired with $LiCoO_2$ cathode) at 1 C and 4 C. Mass loadings of cathode: 13.4 mg cm^{-2}. Mass loadings of anode: 15.7 mg cm^{-2}. *N*/*P* ratio: 1.0.

The volumetric energy density of the pouch cell was calculated by using the following equation: (Cell capacity) × (Average voltage)/ [(Electrode area) × (Thickness of anode including active materials, binder and carbon black)].

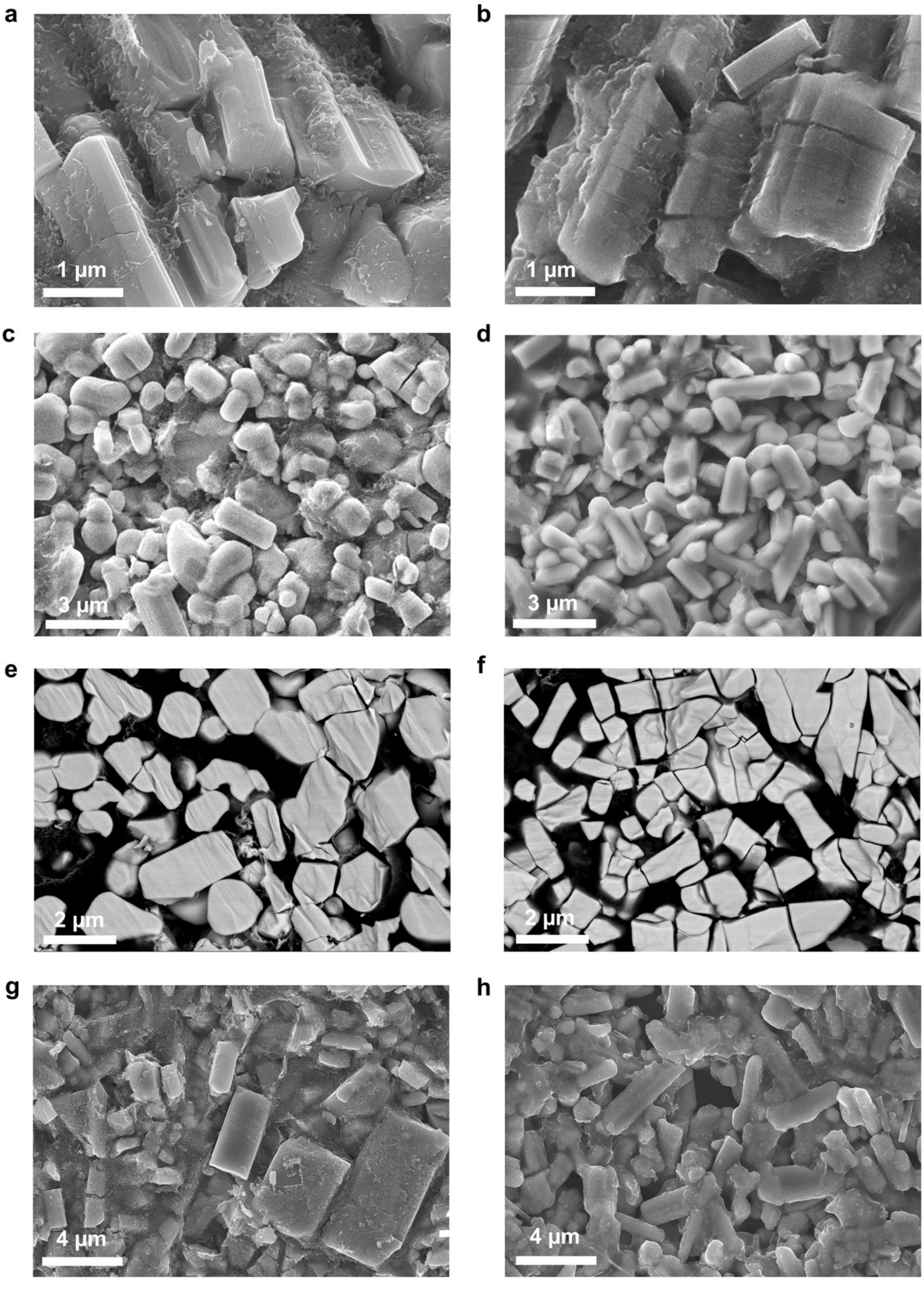

Fig. S19 SEM images of the surface of H-Nb_2O_5 electrodes (a) before and (b) after 1,000 cycles at 6,000 mA g^{-1}, the surface of NPO electrodes (c) before and (d) after 1,000 cycles at 6,000 mA g^{-1}, cross-sectional images of NPO electrodes (e) before and (f) after 1,000 cycles at 6,000 mA g^{-1}, the surface of NWT944 electrodes (g) before and (h) after 7,300 cycles at 6,000 mA g^{-1}.

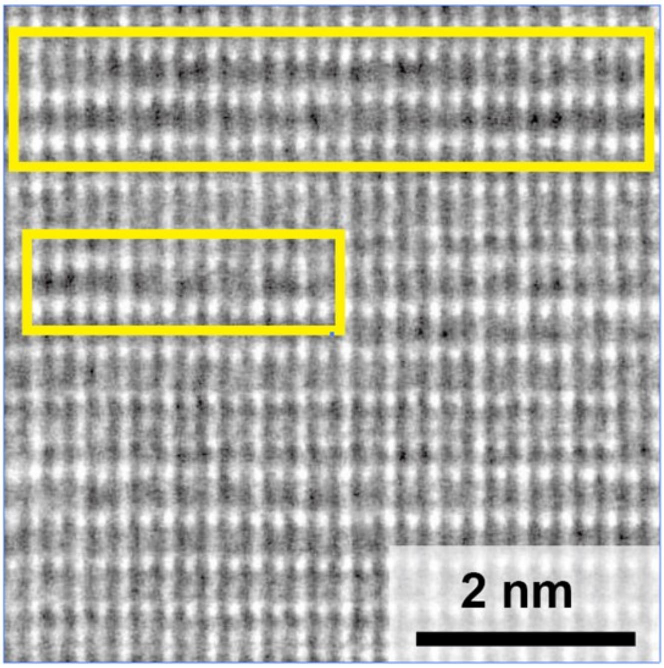

Fig. S20 Stacking fault analysis by using high-resolution STEM-HAADF of H-Nb_2O_5.

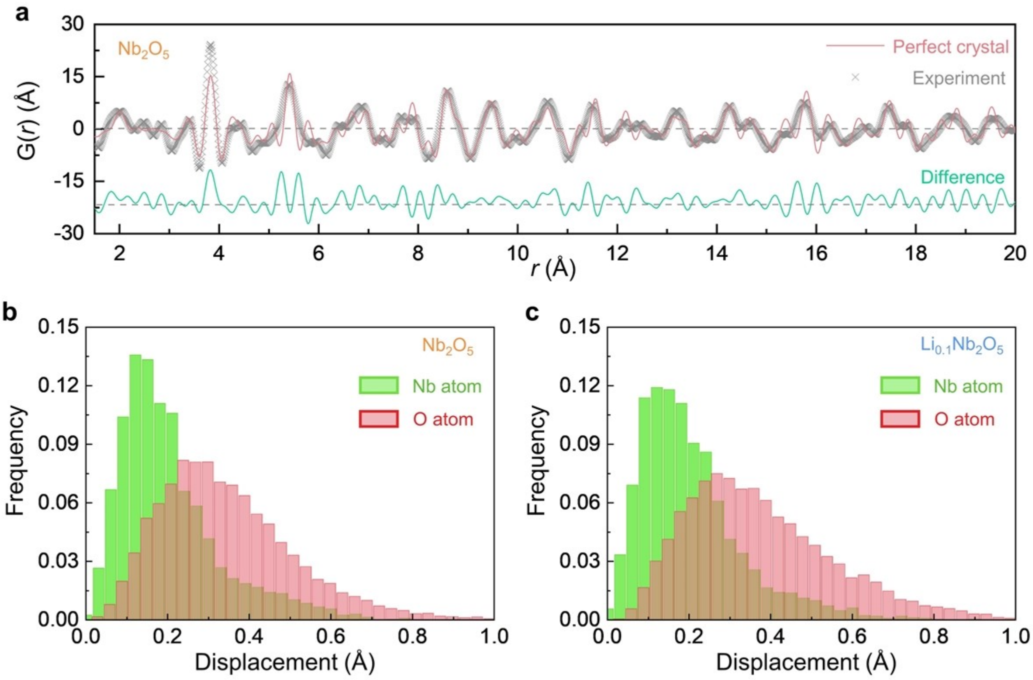

Fig. S21 (a) Pair distribution function (PDF) experimental data for Nb_2O_5 as well as ideal data for the perfect Nb_2O_5 crystal. The distribution of Nb and O displacements for (b) Nb_2O_5 and (c) $Li_{0.1}Nb_2O_5$ compared with the perfect Nb_2O_5 crystal.

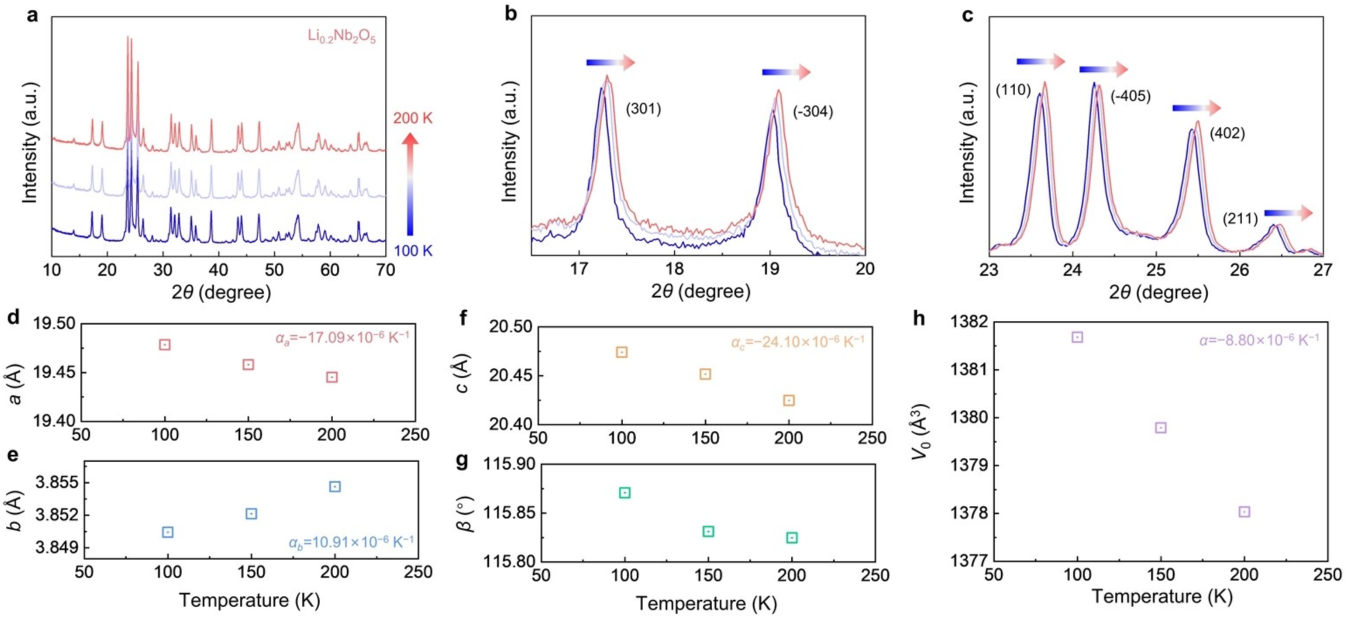

Fig. S22 (a~c) XRD analysis of $Li_{0.2}Nb_2O_5$ at 100 K, 150 K, and 200 K. (d~h) Primary-cell parameters as a function of temperature *T*, together with the calculated coefficient of linear thermal expansion.

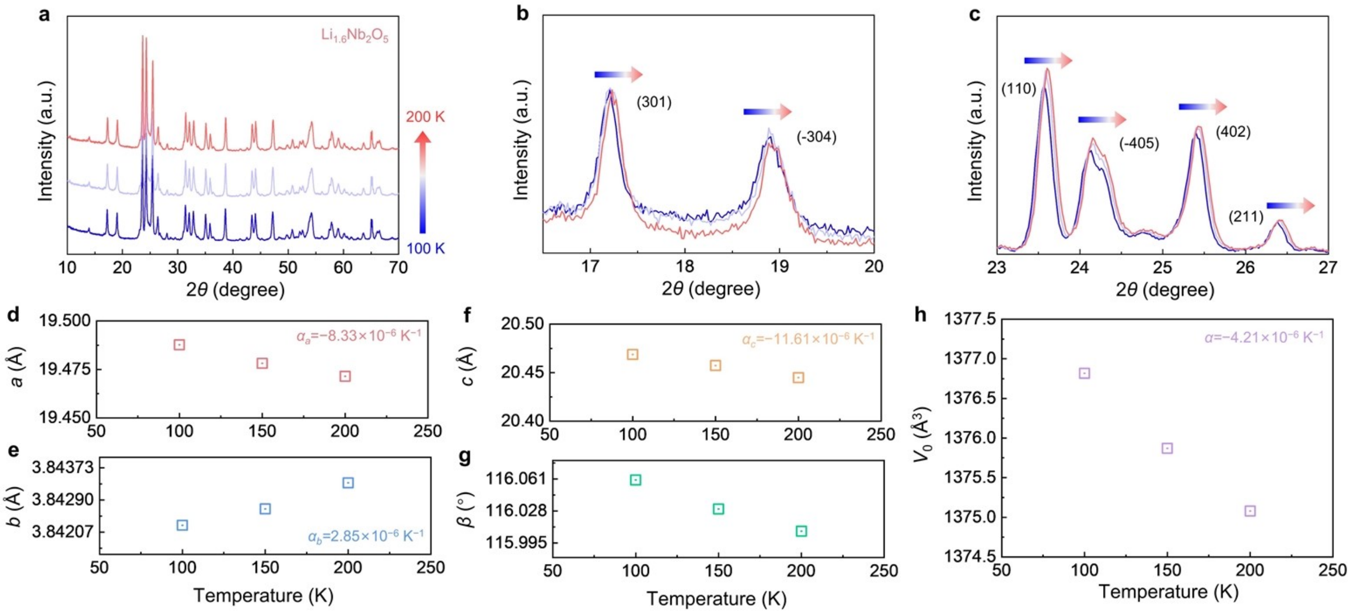

Fig. S23 (a~c) XRD analysis of $Li_{1.6}Nb_2O_5$ at 100 K, 150 K, and 200 K. (d~h) Primary-cell parameters as a function of temperature *T*, together with the calculated coefficient of linear thermal expansion.

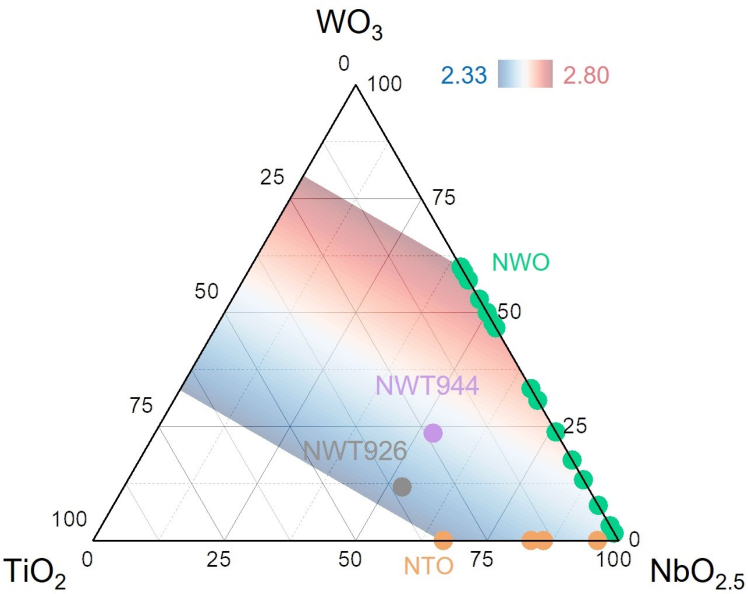

Fig. S24 The calculated pre-zeolite frameworks in the $NbO_{2.5}$-WO_3-TiO_2 phase diagram. The colored area is associated with the Wadsley-Roth structures, with the anion-to-cation ratio from 2.33 to 2.80.

Supplementary Tables

Table S1 Electrochemical comparison table considering characterized particle size, specific surface area, electrode composition, electrode density, high-rate capacity, and cycling capacity retention among Nb_2O_5, H-Nb_2O_5-B, NPO, NWT944, NWT926, and representative Nb-based anodes with high-rate performances. The electrode compositions (mass ratio of active materials: conductive carbon: binder) are listed for references.

Materials	**Characterized size (μm)**	**Surface area (m^2 g^{-1})**	**Electrode composition**	**Electrode density (mg cm^{-2})**	**High-rate capacity (mAh g^{-1})**	**Cycling capacity retention after cycles**	**Refs**
H-Nb_2O_5	**1~5**	**1.3**	**85:9:6**	**1.0~2.0**	**77 (16 A g^{-1})**	**100%, 1,000 cycles (6 A g^{-1})**	**This work**
H-Nb_2O_5-B	**20~50**	**0.8**	**92:4:4**	**2.0~3.0**	**61 (12 A g^{-1})**	**105%, 1,000 cycles (4 A g^{-1})**	**This work**
NPO	**1~3**	**1.1**	**90:4:6**	**1.0~2.0**	**62 (16 A g^{-1})**	**47%, 1,000 cycles (6 A g^{-1})**	**This work**
NWT944	**1~3**	**3.7**	**85:9:6**	**1.0~2.0**	**95 (16 A g^{-1})**	**56%, 15,000 cycles (6 A g^{-1})**	**This work**
NWT926	**1~2**	**4.0**	**85:9:6**	**1.0~2.0**	**92 (16 A g^{-1})**	**80%, 1,000 cycles (6 A g^{-1})**	**This work**
Ag-coated nitridated H-Nb_2O_5	~1.0	N/A	80:10:10	1.5	88 (5 A g^{-1})	~80%, 1,000 cycles (3 A g^{-1})	17
H-Nb_2O_5 with defects	0.5~1.0	1.0	80:10:10	1.0~1.5	86 (16 A g^{-1})	~95%, 2,000 cycles (6 A g^{-1})	18
$KNb_6O_{15}F$-wired Nb_2O_5	0.1~1.0	N/A	70:20:10	~2.0	80 (20 C)	75%, 200 cycles (0.5 C)	19
T-Nb_2O_5/carbide-derived carbon	~0.5	19	80:10:10	1.4	100 (10 A g^{-1})	72%, 500 cycles (0.1 A g^{-1})	20
Hollow and mesoporous T-Nb_2O_5	0.3	N/A	70:20:10	1.0~1.5	125 (50 C)	86%, 2,000 cycles (1 C)	21
M-Nb_2O_5 microspheres	~0.3	N/A	70:20:10	~3.6	122 (5 A g^{-1})	82%, 1,000 cycles (0.2 A g^{-1})	22
T-Nb_2O_5 nanotubes	0.2	39	80:10:10	0.7~1.1	99 (20 C)	~100%, 1,000 cycles (10 C)	23
T-Nb_2O_5 nanoflowers	0.1	N/A	80:10:10	1.2~2.0	130 (5 A g^{-1})	83%, 400 cycles (1 A g^{-1})	24
T-Nb_2O_{5-x}	0.05~0.1	N/A	70:20:10	2.0~4.0	107 (25 C)	~90%, 1,100 cycles (5 C)	25
3D T-Nb_2O_5 microspheres	0.01~0.1	56.2	70:20:10	N/A	113 (3.2 A g^{-1})	86%, 1,000 cycles (0.8 A g^{-1})	26
T-Nb_2O_5@C nanoparticles	<0.1	214.4	80:10:10	2.0	177 (6 A g^{-1})	87.9%, 2,000 cycles (2 A g^{-1})	27
M-Nb_2O_5@ graphene sheets	0.015~0.07	>100	85:10:5	N/A	509 C g^{-1} (20 A g^{-1})	~88%, 2,000 cycles (1 A g^{-1})	28
Nanosheets $Nb_{12}O_{29}$ microspheres	0.05	12.9	65:25:10	1.4	179 (20 C)	96.5%, 500 cycles (10 C)	29
Mesoporous T-Nb_2O_5 nanotubes	0.03	23.7	80:10:10	1.5	70 (5 A g^{-1})	~90%, 5,000 cycles (3 A g^{-1})	30
T-Nb_2O_5 quantum dots in carbon	0.005	268	80:10:10	~1.0	105 (5 A g^{-1})	70%, 1,000 cycles (1 A g^{-1})	31
3D T-Nb_2O_5 nanosheets@C	0.015	N/A	80:10:10	1.2	144 (5 A g^{-1})	95%, 1,000 cycles (2 A g^{-1})	32
3D holey-graphene T-Nb_2O_5	0.015	83	80:10:10	6.0	92 (50 C)	90%, 10,000 cycles (10 C)	33
T-Nb_2O_5 nanowires/graphene	0.01	N/A	93.5:6.5:0	N/A	95 (5 A g^{-1})	~100%, 1,000 cycles (5 A g^{-1})	34

3D porous carbon nanowebs T-Nb_2O_5	~0.01	103	80:10:10	1.0	82 (10 A g^{-1})	88%, 70,000 cycles (1 A g^{-1})	35
TT-Nb_2O_5/CNT films	0.007	N/A	75:15:10	N/A	83 (2 A g^{-1})	66%, 1,000 cycles (5 A g^{-1})	36
T-Nb_2O_5/rGO	0.005	80	70:20:10	1.1~1.5	134 (25 C)	87%, 1,000 cycles (5 C)	37
PNb_9O_{25}	N/A	N/A	75:15:10	1.5	30 (60 C)	86%, 500 cycles (2 C)	38
PNb_9O_{25} nanofiber	0.1~0.5 (dia.)	N/A	80:10:10	1.0~1.4	181 (6 C)	71%, 500 cycles (6 C)	39
$Cu_{0.02}Ti_{0.94}Nb_{2.04}O_7$	4.0	0.7	65:25:10	1.0	182 (10 C)	99%, 1,000 cycles (10 C)	40
Coarse-grained $Mo_xTi_{1-x}Nb_2O_{7+y}$	1~2	1.1	90:5:5	1~2	158 (6 A g^{-1})	75%, 500 cycles (2 A g^{-1})	41
$TiNb_{24}O_{62}$ nanowires	0.3	8.3	80:10:10	1.0~1.5	177 (6 C)	92%, 900 cycles (10 C)	42
Porous $TiNb_2O_7$ nanotubes	0.3	151	70:20:10	N/A	180 (100 C)	86%, 700 cycles (50 C)	43
1D $TiNb_2O_{7-x}$@C fibers	0.2	6.7	90:5:5	11	32 (6 C)	78%, 100 cycles (0.3 C)	44
$TiNb_2O_7$ hollow nanofiber	0.2	N/A	80:10:10	1.5	200 (10 C)	81%, 900 cycles (10 C)	45
Porous $TiNb_2O_7$ nanotubes	0.2	50.2	80:10:10	N/A	116 (30 C)	88%, 500 cycles (5 C)	46
$Ti_2Nb_{10}O_{29}$@TiC/C	0.05~0.08	N/A	100:0:0	0.8	165 (100 C)	66%, 10,000 cycles (10 C)	47
N-doped graphene $TiNb_2O_{7-x}$	0.06	N/A	70:20:10	1.3~1.5	89 (100 C)	87%, 2,000 cycles (10 C)	48
3D/2D cross-linked $Ti_2Nb_{10}O_{29-x}$@C	0.05	N/A	80:10:10	2.0	197 (20 C)	99%, 500 cycles (10 C)	49
$TiNb_2O_7$ microspheres	~0.05	19.8	85:15:5	N/A	142 (100 C)	90%, 1,000 cycles (5 C)	50
Porous $Ti_2Nb_{10}O_{29}$ microspheres	~0.05	19.4	70:20:10	N/A	193 (50 C)	~100%, 1,000 cycles (10 C)	51
TiO_2/Nb_2O_5/$TiNb_2O_7$	0.05	25.4	60:25:15	N/A	185 (5 C)	95%, 1,800 cycles (5 C)	52
Microporous $TiNb_2O_7$	0.05	27	70:20:10	1.5	99 (100 C)	82%, 1,000 cycles (10 C)	53
2D $Ti_2Nb_{10}O_{29}$	0.04~0.05	55	70:20:10	1.5	144 (40 C)	82%, 1,000 cycles (10 C)	54
Vertical graphene/$TiNb_2O_7$@S–C	0.02~0.04	N/A	100:0:0	0.9	181 (160 C)	78%, 5,000 cycles (10 C)	55
Porous $Ti_2Nb_{10}O_{29}$ microspheres	0.02~0.05	25.1	65:25:10	2.0	208 (20 C)	90%, 500 cycles (10 C)	56
$Ti_2Nb_{10}O_{29-x}$@C	0.01~0.05	N/A	65:25:10	N/A	165 (40 C)	98%, 500 cycles (10 C)	57
Highly porous $TiNb_2O_7$	~0.02	48	75:15:10	1.5~2.0	160 (100 C)	84%, 1,000 cycles (5 C)	58
Cr^{3+}-$Ti_2Nb_{10}O_{29}$@ graphene@TiC–C arrays	0.01	N/A	100:0:0	2.0	220 (40 C)	91%, 500 cycles (10 C)	59
Mesostructured $TiNb_2O_7$	0.015	74	70:20:10	1.1~1.4	116 (50 C)	81%, 2,000 cycles (10 C)	60
Coarse-grained $Nb_{18}W_{16}O_{93}$	5.0	N/A	80:10:10	2~3	72 (100 C)	95%, 750 cycles (20 C)	61
$WNb_{12}O_{33}$ nanowires	0.2	N/A	80:10:10	1.5	146 (0.7 A g^{-1})	86%, 700 cycles (0.7 A g^{-1})	62
$W_3Nb_{14}O_{44}$ nanowires	0.4	N/A	80:10:10	N/A	138 (0.7 A g^{-1})	64%, 1,000 cycles (1 A g^{-1})	63
Coarse-grained $FeNb_{11}O_{29}$	0.2~20	0.2	65:25:10	1.4	145 (10 C)	93%, 200 cycles (10 C)	64

Coarse-grained $Cr_{0.2}Fe_{0.8}Nb_{11}O_{29}$	0.2~20	0.3	65:25:10	N/A	123 (10 C)	87%, 500 cycles (10 C)	65
Coarse-grained $HfNb_{24}O_{62}$	2~10	0.4	65:25:10	N/A	105 (10 C)	87%, 500 cycles (10 C)	66
Coarse-grained $Cu_2Nb_{34}O_{87}$	1~10	0.8	65:25:10	N/A	184 (10 C)	89%, 1,000 cycles (10 C)	67
Coarse-grained $AlNb_{11}O_{29}$	~1.0	3.0	89:7:4	8.0	163 (5 C)	80%, 450 cycles (0.5 C)	68
$FeNb_{11}O_{29}$@N	0.2~0.9	N/A	70:20:10	1.5~2.0	44 (100 C)	88%, 10,000 cycles (20 C)	69
$Zr_2Nb_{34}O_{87}$ nanofibers	0.1~0.3	18.4	65:25:10	1.0	86 (10 C)	99%, 1,000 cycles (5 C)	70
$GaNb_{11}O_{29}$ nanowebs	0.25	10.3	65:25:10	N/A	175 (10 C)	87%, 1,000 cycles (10 C)	71
$Cu_2Nb_{34}O_{87}$ nanowires	0.25	N/A	80:10:10	N/A	233 (1.5 A g^{-1})	89%, 300 cycles (0.3 A g^{-1})	72
$FeNb_{11}O_{29}$ nanotubes	0.2	N/A	80:10:10	N/A	54 (50 C)	75%, 2,000 cycles (1 C)	73
$AlNb_{11}O_{29}$ nanowires	0.16	9.7	65:25:10	1.4	131 (10 C)	93%, 500 cycles (10 C)	74
$ZrNb_{14}O_{37}$ nanowires	0.12	N/A	80:10:10	2	168 (0.7 A g^{-1})	74%, 1,000 cycles (0.1 A g^{-1})	75
$ZrNb_{24}O_{62}$ nanowires	0.05	34.9	65:25:10	1.4	182 (30 C)	90%, 1,500 cycles (10 C)	76
Porous $MoNb_{12}O_{33}$ microspheres	0.1	13.1	65:25:10	1.0	138 (10 C)	96%, 1,000 cycles (5 C)	77
$CrNb_{11}O_{29}$ nanorods	0.03~0.05	22.3	65:25:10	N/A	228 (10 C)	91%, 400 cycles (10 C)	78
Porous $Al_{0.5}Nb_{24.5}O_{62}$ microspheres	0.03~0.04	8.3	65:25:10	1.5	192 (10 C)	90%, 500 cycles (10 C)	79

Table S2 Crystallographic information of NWT926.

Phase: Monoclinic

Space Group: *C*2/*c* (No. 15). 162 atoms per unit cell

Lattice Parameters:
a=31.439 Å, *b*=3.866 Å, *c*=20.901 Å, *α*=90.000°, *β*=112.990°, *γ*=90.000°, *V*=2338.516 Å^3

Atom	*x*	*y*	*z*	Occupancy
Nb1	0.066	0.000	0.037	0.529
W1	0.066	0.000	0.037	0.118
Ti1	0.066	0.000	0.037	0.353
Nb2	0.067	0.000	0.224	0.529
W2	0.067	0.000	0.224	0.118
Ti2	0.067	0.000	0.224	0.353
Nb3	0.064	0.500	0.356	0.529
W3	0.064	0.500	0.356	0.118
Ti3	0.064	0.500	0.356	0.353
Nb4	0.202	0.000	0.119	0.529
W4	0.202	0.000	0.119	0.118
Ti4	0.202	0.000	0.119	0.353
Nb5	0.201	0.000	0.302	0.529
W5	0.201	0.000	0.302	0.118
Ti5	0.201	0.000	0.302	0.353
Nb6	0.200	0.500	0.433	0.529
W6	0.200	0.500	0.433	0.118
Ti6	0.200	0.500	0.433	0.353
O1	0.000	0.000	0.000	0.986
O2	0.006	0.000	0.195	0.986
O3	0.068	0.000	0.136	0.986
O4	0.071	0.000	0.333	0.986
O5	0.072	0.500	0.057	0.986
O6	0.073	0.500	0.256	0.986
O7	0.067	0.500	0.446	0.986
O8	0.141	0.000	0.075	0.986
O9	0.140	0.000	0.270	0.986
O10	0.141	0.500	0.406	0.986
O11	0.220	0.000	0.031	0.986
O12	0.208	0.000	0.220	0.986
O13	0.204	0.000	0.413	0.986
O14	0.223	0.500	0.134	0.986
O15	0.210	0.500	0.333	0.986

Table S3 Linear CTE (unit: 10^{-6} K^{-1}) of 260 materials[80-83].

No.	Materials	CTE	No.	Materials	CTE	No.	Materials	CTE
1	$MgO\cdot 2PbO\cdot WO_3$	-7.69	31	$Na_{1.5}Zr_{1.5}Cr_{0.5}(PO_4)_3$	0.50	61	$Sr_{0.5}Zr_2(PO_4)_3$	3.16
2	$ZrO_2\cdot 2WO_3$	-7.20	32	$GaNbO_4$	0.50	62	$SrO\cdot Al_2O_3\cdot 2SiO_2$	3.20
3	$NaTi_2(PO_4)_3$	-5.50	33	$2MgO\cdot 2Al_2O_3\cdot 5SiO_2$	0.60	63	$TiTa_{18}O_{47}$	3.24
4	$Ta_2O_5\cdot V_2O_5$	-4.13	34	$2ZnO\cdot GeO_2$	0.67	64	$ZnO\cdot V_2O_5$	3.33
5	$NaZr_2(PO_4)_3$	-4.00	35	$SrO\cdot ZrO_2$	0.75	65	$Co_3(PO_4)_2$	3.33
6	$Li_2O\cdot Al_2O_3\cdot 2SiO_2$	-3.33	36	U_3O_8	0.80	66	$Ba_{0.5}Zr_2(PO_4)_3$	3.37
7	$PbO\cdot TiO_2$	-3.30	37	V_2O_5	0.87	67	RuO_2	3.60
8	$Na_{3/2}Zr_{15/8}(PO_4)_3$	-2.35	38	PNb_9O_{25}	0.97	68	$CaO\cdot HfO_2$	3.60
9	$3PbO\cdot P_2O_5$	-2.33	39	Mo_2O_3	1.10	69	$HfSiO_4$	3.60
10	$Ca_{0.5}Zr_2(PO_4)_3$-NZP	-2.11	40	$Sn_3(PO_4)_2$	1.43	70	$ZrSiO_4$	3.64
11	$Ca_{0.5}Zr_2(PO_4)_3$-CTP	-1.60	41	$TiTa_2O_7$	1.43	71	$Dy_2O_3\cdot 2Al_2O_3$	3.66
12	$AlNb_9O_{24}$	-1.40	42	$Nb_2O_5\cdot V_2O_5$	1.50	72	HfO_2	3.80
13	$Nb_{14}W_3O_{44}$	-1.27	43	$Nb_{11}Ta_2Ti_3O_{41}$	1.50	73	SnO_2	3.80
14	$GeNb_{18}O_{47}$	-1.26	44	$BaNb_6O_{16}$	1.51	74	$K_2O\cdot Nb_2O_5$	3.80
15	$Nb_{12}WO_{33}$	-1.25	45	$TiO_2\cdot Ta_2O_5$	1.57	75	Zn_2SiO_4	3.86
16	$AlNb_{11}O_{29}$	-1.19	46	$Sr_2Nb_{10}O_{27}$	1.61	76	$MgO\cdot 2TiO_2$	3.88
17	$ZrNb_{14}O_{37}$	-1.17	47	TiO	1.67	77	IrO_2	3.89
18	$2Nb_2O_5\cdot Ta_2O_5$	-0.83	48	Ta_2O_5	1.87	78	Ta_2O_5	3.92
19	$GaNb_{11}O_{29}$	-0.82	49	Nb_3BO_9	1.94	79	$AlNbO_4$	3.97
20	Nb_2O_5	-0.70	50	$NbPO_5$	2.00	80	$3MgO\cdot Nb_2O_5$	4.00
21	$Ta_2O_5\cdot Nb_2O_5$	-0.53	51	$Mg_{0.5}Zr_2(PO_4)_3$	2.11	81	$CaCO_3$	4.00
22	$LaNb_5O_{14}$	-0.43	52	$K_2Nb_8O_{21}$	2.13	82	$Ca_{0.25}Na_{0.5}Ti_2(PO_4)_3$	4.00
23	$3CaO\cdot 5Al_2O_3$	-0.40	53	$Li_2Nb_{32}O_{81}$	2.16	83	$BaO\cdot Al_2O_3\cdot 2SiO_2$	4.00
24	$Ti_2Nb_{10}O_{29}$	-0.31	54	$Zn(PO_3)_2$	2.20	84	$NbPO_5$	4.20
25	$2Al_2O_3\cdot 5WO_3$	0.00	55	$Al_2O_3\cdot SiO_2$	2.25	85	$TaPO_5$	4.25
26	$Sr_2O_3\cdot WO_3$	0.00	56	$2Al_2O_3\cdot SiO_2$	2.25	86	ZnO	4.30
27	$NiNb_{14}O_{36}$	0.15	57	$ZrO_2\cdot TiO_2$	2.50	87	$2PbO\cdot P_2O_5$	4.33
28	$2CaO\cdot MgO\cdot WO_3$	0.18	58	WO_2	2.60	88	Y_2SiO_5	4.33
29	$TiNb_2O_7$	0.45	59	$3Al_2O_3\cdot 2SiO_2$	2.63	89	$Ca_{0.5}ZrTi(PO_4)_3$	4.35
30	SiO_2 (Fused)	0.49	60	$Li_2O\cdot Ta_2O_5$	2.66	90	$Mg(PO_3)_2$	4.35

Table S3 Linear CTE (unit: 10^{-6} K^{-1}) of 260 materials (continued).

No.	Materials	CTE	No.	Materials	CTE	No.	Materials	CTE
91	$3PbO\cdot Fe_2O_3\cdot WO_3$	4.38	121	$MgO\cdot Cr_2O_3$	6.20	151	TiO_2	7.50
92	GeO_2 (Rutile)	4.50	122	BeO	6.30	152	$MgCO_3$	7.63
93	$CaAl_2(SiO_4)_2$	4.50	123	Er_2O_3	6.30	153	$8PbO\cdot P_2O_5$	7.67
94	$CaO\cdot 6Al_2O_3$	4.53	124	$Ca_{0.25}Na_{0.5}Zr_2(PO_4)_3$	6.30	154	ThO_2	7.70
95	$CaO\cdot Al_2O_3\cdot SiO_2$	4.53	125	$BaO\cdot TiO_2$	6.30	155	$3CaO\cdot 2SiO_2$	7.72
96	$ZrO_2\cdot Cr_2O_3$	4.62	126	$3PbO\cdot 2Ta_2O_5$	6.50	156	Pr_2O_3	7.80
97	$CaO\cdot Al_2O_3$	4.70	127	Gd_2O_3	6.60	157	$FeCO_3$	7.83
98	$PbO\cdot Al_2O_3$	4.88	128	Sc_2O_3	6.60	158	$4CaO\cdot Al_2O_3\cdot Fe_2O_3$	7.90
99	$Na_2O\cdot Nb_2O_5$	4.97	129	$BaO\cdot ZrO_2$	6.67	159	$CaO\cdot ZrO_2$	7.90
100	$2PbO\cdot GeO_2$	5.00	130	$PbO\cdot P_2O_5$	6.67	160	Fe_3O_4	8.00
101	$Ca_{0.5}Ti_2(PO_4)_3$-CTP	5.10	131	$ThO_2\cdot SiO_2$	6.67	161	PuO_2	8.10
102	VO_2	5.22	132	$3CaO\cdot Al_2O_3$	6.80	162	$Al_2O_3\cdot TiO_2$	8.10
103	$Na_3Cr_2(PO_4)_3$	5.30	133	$4MgO\cdot Nb_2O_5$	6.80	163	$4PbO\cdot SiO_2$	8.10
104	$5CaO\cdot 3Al_2O_3$	5.30	134	$CaO\cdot MgO\cdot 2SiO_2$	6.80	164	$K_2O\cdot 7GeO_2$	8.24
105	$2MgO\cdot Nb_2O_5$	5.33	135	$2MgO\cdot TiO_2$	6.89	165	$2ZnO\cdot V_2O_5$	8.33
106	Al_2O_3	5.40	136	In_2O_3	6.90	166	$BaO\cdot SnO_2$	8.34
107	Lu_2O_3	5.50	137	Tm_2O_3	7.00	167	MnO_2	8.40
108	$SrO\cdot HfO_2$	5.50	138	$MgO\cdot Al_2O_3$	7.00	168	$NiO\cdot TiO_2$	8.58
109	$NiCO_3$	5.51	139	$3PbO\cdot 2P_2O_5$	7.00	169	$MgSiO_3$	8.60
110	$PbO\cdot SiO_2$	5.71	140	$MnSiO_3$	7.00	170	$6HfO_2\cdot Ta_2O_5$	8.62
111	$Li_2Si_2O_5$	5.71	141	$Li(Li_{0.1}Mn_{1.9})O_4$	7.00	171	Cr_2O_3	8.80
112	$NiO\cdot Al_2O_3$	5.79	142	Ho_2O_3	7.10	172	Eu_2O_3	8.80
113	$Cr_2O_3\cdot V_2O_5$	5.79	143	$PbO\cdot WO_3$	7.10	173	ZrO_2	8.80
114	Mn_2O_3	5.80	144	$BaO\cdot TiO_2$	7.14	174	$MgO\cdot Fe_2O_3$	8.80
115	$K_2O\cdot Ta_2O_5$	5.80	145	$Dy_2O_3\cdot Nb_2O_5$	7.25	175	$Zr_5Nb_2O_{15}$	8.94
116	$Zn_3(PO_4)_2$	5.80	146	Y_2O_3	7.30	176	Ti_2O_3	9.00
117	$Zn_2P_2O_7$	5.93	147	$BaO\cdot 4TiO_2$	7.40	177	$2CaO\cdot Fe_2O_3$	9.00
118	$2MgO\cdot 4SiO_2$	6.00	148	$3K_2O\cdot 11GeO_2$	7.42	178	$CdO\cdot ZrO_2$	9.00
119	Yb_2O_3	6.10	149	Dy_2O_3	7.50	179	$2FeO\cdot SiO_2$	9.00
120	$MgO\cdot Nb_2O_5$	6.13	150	SrO	7.50	180	$CaO\cdot FeO\cdot SiO_2$	9.00

Table S3 Linear CTE (unit: 10^{-6} K^{-1}) of 260 materials (continued).

No.	Materials	CTE	No.	Materials	CTE	No.	Materials	CTE
181	Mg_2SiO_4	9.00	211	La_2O_3	10.80	241	Na_2SO_4	15.10
182	$MnO\cdot Al_2O_3$	9.13	212	$CaO\cdot MoO_3$	10.90	242	$PbO\cdot Ta_2O_5$	16.10
183	$ZnO\cdot Al_2O_3$	9.20	213	$CaO\cdot MgO\cdot SiO_2$	10.90	243	WO_3	16.40
184	$PbO\cdot ZrO_2$	9.20	214	Nd_2O_3	11.00	244	BaO	17.80
185	Sm_2O_3	9.24	215	$Li_2O\cdot Nb_2O_5$	11.10	245	$NH_4H_2AsO_4$	18.20
186	GeO_2 (Quartz)	9.30	216	CaO	11.20	246	$Li_2O\cdot Na_2O\cdot 2P_2O_5$	20.00
187	$MnCO_3$	9.30	217	$MgO\cdot 2FeO$	11.20	247	$Ba(NO_3)_2$	20.80
188	UO_2	9.40	218	$CaO\cdot Fe_2O_3$	11.40	248	$Gd_2O_3\cdot 3MoO_3$	21.00
189	$2PbO\cdot Ta_2O_5$	9.40	219	$2BaO\cdot SrO\cdot WO_3$	11.50	249	$Na_2O\cdot WO_3$	21.10
190	$CaO\cdot SiO_2$	9.40	220	$PrO_{1.83}(Pr_6O_{11})$	11.58	250	Li_2SO_4	21.60
191	CeO_2	9.50	221	$CaO\cdot WO_3$	11.80	251	$Na_2O\cdot La_2O_3\cdot 4MoO_3$	21.70
192	$3CaO\cdot SiO_2$	9.50	222	FeO	12.00	252	Na_2CaSiO_4	21.70
193	Ni_2SiO_4	9.50	223	$5PbO\cdot GeO_2\cdot P_2O_5$	12.00	253	$5PbO\cdot B_2O_3\cdot SiO_2$	21.90
194	$2CaO\cdot MgO\cdot 2SiO_2$	9.60	224	CoO	12.20	254	$NaD_3(SeO_3)_2$	22.00
195	Co_2SiO_4	9.60	225	$LiFePO_4$	12.20	255	KD_2AsO_4	25.60
196	$CoO\cdot TiO_2$	9.63	226	$LiTi_2(PO_4)_3$	12.20	256	$La_{0.6}Li_{0.2}TiO_3$	26.60
197	$2BaO\cdot CaO\cdot WO_3$	9.72	227	KH_2PO_4	12.30	257	RbD_2AsO_4	26.60
198	Fe_2O_3	9.90	228	$AlPO_4$	12.50	258	$KH_3(SeO_3)_2$	28.10
199	$3ZnO\cdot V_2O_5$	10.00	229	$LiNi_{0.33}Mn_{0.33}Co_{0.33}O_2$	12.50	259	RbH_2AsO_4	29.60
200	$2FeO\cdot 2SiO_2$	10.00	230	MnO	12.70	260	$NaH_3(SeO_3)_2$	30.00
201	$SrO\cdot MoO_3$	10.10	231	$2CaO\cdot SiO_2$	12.80			
202	NiO	10.20	232	$NaAlSiO_4$	13.00			
203	$CoCO_3$	10.20	233	$Li_7La_3Zr_2O_{12}$	13.00			
204	SiO_2 (Crystalline)	10.30	234	$LiCoO_2$	13.00			
205	$SrO\cdot TiO_2$	10.30	235	CdO	13.20			
206	$YNbO_4$	10.40	236	EuO	13.50			
207	MgO	10.50	237	$K_2O\cdot 2GeO_2$	13.60			
208	VPO_5	10.50	238	$CsAl(SiO_3)_2$	13.60			
209	$2PbO\cdot SiO_2$	10.50	239	Li_4SiO_4	15.00			
210	$5PbO\cdot 2P_2O_5$	10.67	240	$Li_4Ti_5O_{12}$	15.00			

Table S4 Particle sizes and electrode densities of H-Nb_2O_5, H-Nb_2O_5-B, NPO, NTO, NWO, NWT944, NWT926, $Li_4Ti_5O_{12}$, and meso-carbon microbeads.

Materials	Characterized particle size (μm)	Electrode density (g cm^{-3})	Initial Coulombic efficiency (%)
H-Nb_2O_5	1~5	3.1	96.1
H-Nb_2O_5-B	20~50	3.7	97.0
NPO	1~3	3.3	97.2
TNO	~1	2.7	97.3
NWO	2~10	3.8	94.8
NWT944	1~3	3.2	96.5
NWT926	1~2	3.3	96.0
$Li_4Ti_5O_{12}$	0.8~3.0	2.5	97.0
Meso-carbon microbeads	16~19	2.0	88.5

Table S5 Comparison of the electrochemical properties among H-Nb_2O_5, H-Nb_2O_5-B, NPO, NTO, NWO, NWT944, NWT926. Capacity measured at 200 mA g^{-1}, rate retention defined as the ratio of capacity at 6,000 mA g^{-1} (12 mA cm^{-2}) to capacity at 200 mA g^{-1}, voltage defined as average discharge voltage at 200 mA g^{-1}, gravimetric and volumetric energy density defined as the anode side (including active material, conductive carbon, and binder) in the full cells using $LiNi_{0.5}Mn_{1.5}O_4$ as the cathode, and cyclability defined as capacity retention after 1,000 cycles at 12 mA cm^{-2} (~60 C).

Materials	Capacity at 200 mA g^{-1} (mAh g^{-1})	Rate retention at 12 mA cm^{-2} (%)	Voltage (V vs. Li$^+$/Li)	Gravimetric energy density at 12 mA cm^{-2} (Wh kg^{-1})	Volumetric energy density at 12 mA cm^{-2} (Wh L^{-1})	Capacity retention after 1000 cycles at 12 mA cm^{-2} (%)
H-Nb_2O_5	192.2	60.4	1.54	364	1,128	99.7
H-Nb_2O_5-B	215.9	54.3	1.60	360	1,333	104.6
NPO	209.9	69.4	1.53	470	1,550	46.8
NTO	236.3	60.1	1.50	465	1,256	69.0
NWO	180.2	69.6	1.68	394	1,499	36.1
NWT944	204.2	67.4	1.62	422	1,350	88.7
NWT926	187.1	59.0	1.57	343	1,133	79.5

Table S6 Comparison of diffusion coefficient at 390 K, calculated activation energy and pre-A factor for the $Li_xNb_{16}W_5O_{55}$ (x = 6.3, 8.4) and $Li_xNb_{18}W_{16}O_{93}$ (x = 3.4, 6.8, 10.2) in reference[61].

Materials	Diffusion coefficient at 390 K ($m^2\ s^{-1}$)	Activation energy (meV)	Pre-A factor
$Li_{6.3}Nb_{16}W_5O_{55}$	4.1×10^{-13}	54.2	2.2×10^{-5}
$Li_{8.4}Nb_{16}W_5O_{55}$	5.6×10^{-13}	56.6	2.5×10^{-5}
$Li_{3.4}Nb_{18}W_{16}O_{93}$	1.5×10^{-12}	101.5	1.5×10^{-4}
$Li_{6.8}Nb_{18}W_{16}O_{93}$	1.1×10^{-12}	139.5	3.9×10^{-4}
$Li_{10.2}Nb_{18}W_{16}O_{93}$	1.7×10^{-12}	126.2	3.4×10^{-4}

Table S7 Details of electrochemical measurements for H-Nb_2O_5, H-Nb_2O_5-B, NPO, NTO, NWO, NWT944, NWT926, $Li_4Ti_5O_{12}$, meso-carbon microbeads, $LiCoO_2$, and $LiNi_{0.33}Co_{0.33}Mn_{0.33}O_2$, $LiNi_{0.6}Co_{0.2}Mn_{0.2}O_2$, $LiNi_{0.5}Mn_{1.5}O_4$, and $LiFePO_4$. The listed electrode compositions are the mass ratio of active materials: conductive carbon: binder.

Materials	Electrode composition	Active material loading (mg cm^{-2})	Half-cell cycling window (vs. Li^+/Li)	GITT titration time (mins)	GITT relaxation time (mins)
H-Nb_2O_5	85:9:6	1.0~2.0 5.0~11.0 (full cells)	1.0~2.5	50	900
H-Nb_2O_5-B	92:4:4	2.0~3.0 2.0~16.0 (different mass loading analysis) 15.0~16.0 (full cells)	1.0~2.5	50	900
NPO	90:4:6	1.0~2.0	1.0~2.5	50	900
TNO	90:4:6	1.0~2.0	1.0~2.5	60	900
NWO	85:7.5:7.5	1.0~2.0	1.0~3.0	50	900
NWT944	85:9:6	1.0~2.0	1.0~3.0	50	900
NWT926	85:9:6	1.0~2.0	1.0~3.0	50	900
$Li_4Ti_5O_{12}$	85:7.5:7.5	1.0~2.0	1.0~2.5	/	/
Meso-carbon microbeads	90:5:5	1.0~2.0	0.01~2.5	/	/
$LiCoO_2$	90:5:5	1.0~2.0 13.0~14.0 (full cells)	3.1~4.4	25	480
$LiNi_{0.33}Co_{0.33}Mn_{0.33}O_2$	90:5:5	1.0~2.0	3.1~4.4	50	900
$LiNi_{0.6}Co_{0.2}Mn_{0.2}O_2$	85:7.5:7.5	8.0~10.0 (full cells)	3.1~4.4	/	/
$LiNi_{0.5}Mn_{1.5}O_4$	85:7.5:7.5	1.0~2.0 13.0~14.0 (full cells)	3.4~4.9	/	/
$LiFePO_4$	85:7.5:7.5	1.0~2.0 7.0~8.0 (full cells)	2.0~4.3	/	/

Supplementary References

1. T. Degen, M. Sadki, E. Bron, U. König and G. Nénert, *Powder Diffr.*, 2014, **29**, 13-18.
2. J. Rodriguez-Carvajal, *Satellite meeting on powder diffraction of the XV congress of the IUCr*, *Toulouse, France,* 1990, 127.
3. A. P. Hammersley, S. O. Svensson, M. Hanfland, A. N. Fitch and D. Hausermann, *High Press. Res.*, 1996, **14**, 235-248.
4. X. Qiu, J. W. Thompson and S. J. Billinge, *J. Appl. Crystallogr.*, 2004, **37**, 678-678.
5. C. Ophus, J. Ciston and C. T. Nelson, *Ultramicroscopy*, 2016, **162**, 1-9.
6. B. H. Savitzky, S. E. Zeltmann, L. A. Hughes, H. G. Brown, S. Zhao, P. M. Pelz, T. C. Pekin, E. S. Barnard, J. Donohue, L. Rangel DaCosta, E. Kennedy, Y. Xie, M. T. Janish, M. M. Schneider, P. Herring, C. Gopal, A. Anapolsky, R. Dhall, K. C. Bustillo, P. Ercius, M. C. Scott, J. Ciston, A. M. Minor and C. Ophus, *Microsc. Microanal.*, 2021, **27**, 712-743.
7. G. Kresse and D. Joubert, *Phys. Rev. B*, 1999, **59**, 1758.
8. G. Kresse and J. Furthmüller, *Comput. Mater. Sci.*, 1996, **6**, 15-50.
9. J. P. Perdew, K. Burke and M. Ernzerhof, *Phys. Rev. Lett.*, 1996, **77**, 3865.
10. G. Kresse and J. Furthmüller, *Phys. Rev. B*, 1996, **54**, 11169.
11. G. Henkelman, B. P. Uberuaga and H. Jónsson, *J. Chem. Phys.*, 2000, **113**, 9901-9904.
12. K. Momma and F. Izumi, *J. Appl. Crystallogr.*, 2011, **44**, 1272-1276.
13. M. G. Tucker, D. A. Keen, M. T. Dove, A. L. Goodwin and Q. Hui, *J. Phys. Condens. Matter.*, 2007, **19**, 335218.
14. Q. Gao, J. Wang, A. Sanson, Q. Sun, E. Liang, X. Xing and J. Chen, *J. Am. Chem. Soc.*, 2020, **142**, 6935-6939.
15. R. Li, Y. Qin, X. Liu, L. Yang, C. Lin, R. Xia, S. Lin, Y. Chen and J. Li, *Electrochim. Acta*, 2018, **266**, 202-211.
16. Z. Song, H. Li, W. Liu, H. Zhang, J. Yan, Y. Tang, J. Huang, H. Zhang and X. Li, *Adv. Mater.*, 2020, **32**, 2001001.
17. J. Y. Cheong, C. Kim, J. W. Jung, K. R. Yoon, S. H. Cho, D. Y. Youn, H. Y. Jang and I. D. Kim, *Small*, 2017, **13**, 1603610.
18. T. Li, G. Nam, K. Liu, J.-H. Wang, B. Zhao, Y. Ding, L. Soule, M. Avdeev, Z. Luo, W. Zhang, T. Yuan, P. Jing, M. G. Kim, Y. Song and M. Liu, *Energy Environ. Sci.*, 2022, **15**, 254-264.
19. D. Cao, Z. Yao, J. Liu, J. Zhang and C. Li, *Energy Storage Mater.*, 2018, **11**, 152-160.
20. Ö. Budak, M. Geißler, D. Becker, A. Kruth, A. Quade, R. Haberkorn, G. Kickelbick, B. J. M. Etzold and V. Presser, *ACS Appl. Mater. Interfaces*, 2020, **3**, 4275-4285.
21. Y. G. Sun, J. Y. Piao, L. L. Hu, D. S. Bin, X. J. Lin, S. Y. Duan, A. M. Cao and L. J. Wan, *J. Am. Chem. Soc.*, 2018, **140**, 9070-9073.
22. Z. Hu, Q. He, Z. Liu, X. Liu, M. Qin, B. Wen, W. Shi, Y. Zhao, Q. Li and L. Mai, *Sci. Bull.*, 2020, **65**, 1154-1162.
23. N. Li, X. Lan, L. Wang, Y. Jiang, S. Guo, Y. Li and X. Hu, *ACS Appl. Mater. Interfaces*, 2021, **13**, 16445-16453.
24. F. Su, J. Qin, P. Das, F. Zhou and Z.-S. Wu, *Energy Environ. Sci.*, 2021, **14**, 2269-2277.
25. Y. Zheng, Z. Yao, Z. Shadike, M. Lei, J. Liu and C. Li, *Adv. Funct. Mater.*, 2021, **32**, 2107060.
26. Z. Chen, H. Li, X. Lu, L. Wu, J. Jiang, S. Jiang, J. Wang, H. Dou and X. Zhang, *ChemElectroChem*, 2018, **5**, 1516-1524.
27. J. Meng, Q. He, L. Xu, X. Zhang, F. Liu, X. Wang, Q. Li, X. Xu, G. Zhang, C. Niu, Z. Xiao, Z. Liu, Z. Zhu, Y. Zhao and L. Mai, *Adv. Energy Mater.*, 2019, **9**, 1802695.
28. L. Kong, X. Cao, J. Wang, W. Qiao, L. Ling and D. Long, *J. Power Sources*, 2016, **309**, 42-49.
29. R. Li, X. Zhu, Q. Fu, G. Liang, Y. Chen, L. Luo, M. Dong, Q. Shao, C. Lin, R. Wei and Z. Guo, *Chem. Commun.*, 2019, **55**, 2493-2496.
30. J. Y. Cheong, J.-W. Jung, D.-Y. Youn, C. Kim, S. Yu, S.-H. Cho, K. R. Yoon and I.-D. Kim, *J. Power Sources*, 2017,

360, 434-442.

31. S. Liu, J. Zhou, Z. Cai, G. Fang, Y. Cai, A. Pan and S. Liang, *J. Mater. Chem. A*, 2016, **4**, 17838-17847.
32. Y. Li, Y. Wang, G. Cui, T. Zhu, J. Zhang, C. Yu, J. Cui, J. Wu, H. H. Tan, Y. Zhang and Y. Wu, *ACS Appl. Energy Mater.*, 2020, **3**, 12037-12045.
33. H. Sun, L. Mei, J. Liang, Z. Zhao, C. Lee, H. Fei, M. Ding, J. Lau, M. Li, C. Wang, X. Xu, G. Hao, B. Papandrea, I. Shakir, B. Dunn, Y. Huang and X. Duan, *Science*, 2017, **356**, 599-604.
34. H. Song, J. Fu, K. Ding, C. Huang, K. Wu, X. Zhang, B. Gao, K. Huo, X. Peng and P. K. Chu, *J. Power Sources*, 2016, **328**, 599-606.
35. M. Y. Song, N. R. Kim, H. J. Yoon, S. Y. Cho, H. J. Jin and Y. S. Yun, *ACS Appl. Mater. Interfaces*, 2017, **9**, 2267-2274.
36. J. Kang, H. Zhang, Z. Zhan, Y. Li, M. Ling and X. Gao, *ACS Appl. Mater. Interfaces*, 2020, **3**, 11841-11847.
37. X. Han, P. A. Russo, C. Triolo, S. Santangelo, N. Goubard‐Bretesché and N. Pinna, *ChemElectroChem*, 2020, **7**, 1689-1698.
38. M. B. Preefer, M. Saber, Q. Wei, N. H. Bashian, J. D. Bocarsly, W. Zhang, G. Lee, J. Milam-Guerrero, E. S. Howard, R. C. Vincent, B. C. Melot, A. Van der Ven, R. Seshadri and B. S. Dunn, *Chem. Mater.*, 2020, **32**, 4553-4563.
39. H. Yu, J. Zhang, M. Xia, C. Deng, X. Zhang, R. Zheng, S. Chen, J. Shu and Z.-B. Wang, *J. Materiomics*, 2020, **6**, 781-787.
40. C. Yang, C. Lin, S. Lin, Y. Chen and J. Li, *J. Power Sources*, 2016, **328**, 336-344.
41. L. Zhao, S. Wang, Y. Dong, W. Quan, F. Han, Y. Huang, Y. Li, X. Liu, M. Li, Z. Zhang, J. Zhang, Z. Tang and J. Li, *Energy Storage Mater.*, 2021, **34**, 574-581.
42. H. Yu, X. Cheng, H. Zhu, R. Zheng, T. Liu, J. Zhang, M. Shui, Y. Xie and J. Shu, *Nano Energy*, 2018, **54**, 227-237.
43. H. Park, D. H. Shin, T. Song, W. I. Park and U. Paik, *J. Mater. Chem. A*, 2017, **5**, 6958-6965.
44. T. Tian, L. L. Lu, Y. C. Yin, F. Li, T. W. Zhang, Y. H. Song, Y. H. Tan and H. B. Yao, *Adv. Funct. Mater.*, 2020, **31**, 2007419.
45. H. Yu, H. Lan, L. Yan, S. Qian, X. Cheng, H. Zhu, N. Long, M. Shui and J. Shu, *Nano Energy*, 2017, **38**, 109-117.
46. H. Li, L. Shen, J. Wang, S. Fang, Y. Zhang, H. Dou and X. Zhang, *J. Mater. Chem. A*, 2015, **3**, 16785-16790.
47. Z. Yao, X. Xia, S. Zhang, C.-a. Zhou, G. Pan, Q. Xiong, Y. Wang, X. Wang and J. Tu, *Energy Storage Mater.*, 2020, **25**, 555-562.
48. Y. Yang, J. Huang, Z. Cao, Z. Lv, D. Wu, Z. Wen, W. Meng, J. Zeng, C. C. Li and J. Zhao, *Adv Sci (Weinh)*, 2022, **9**, e2104530.
49. S. Deng, H. Zhu, G. Wang, M. Luo, S. Shen, C. Ai, L. Yang, S. Lin, Q. Zhang, L. Gu, B. Liu, Y. Zhang, Q. Liu, G. Pan, Q. Xiong, X. Wang, X. Xia and J. Tu, *Nat. Commun.*, 2020, **11**, 132.
50. H. Park, H. B. Wu, T. Song, X. W. David Lou and U. Paik, *Adv. Energy Mater.*, 2015, **5**, 1401945.
51. S. Lou, X. Cheng, J. Gao, Q. Li, L. Wang, Y. Cao, Y. Ma, P. Zuo, Y. Gao, C. Du, H. Huo and G. Yin, *Energy Storage Mater.*, 2018, **11**, 57-66.
52. G. Wang, Z. Wen, L. Du, Y.-E. Yang, S. Li, J. Sun and S. Ji, *J. Power Sources*, 2017, **367**, 106-115.
53. S. Lou, X. Cheng, Y. Zhao, A. Lushington, J. Gao, Q. Li, P. Zuo, B. Wang, Y. Gao, Y. Ma, C. Du, G. Yin and X. Sun, *Nano Energy*, 2017, **34**, 15-25.
54. S. Shen, S. Zhang, S. Deng, G. Pan, Y. Wang, Q. Liu, X. Wang, X. Xia and J. Tu, *J. Mater. Chem. A*, 2019, **7**, 22958-22966.
55. S. Shen, W. Guo, D. Xie, Y. Wang, S. Deng, Y. Zhong, X. Wang, X. Xia and J. Tu, *J. Mater. Chem. A*, 2018, **6**, 20195-20204.

56. X. Xia, S. Deng, S. Feng, J. Wu and J. Tu, *J. Mater. Chem. A*, 2017, **5**, 21134-21139.
57. S. Deng, Y. Zhang, D. Xie, L. Yang, G. Wang, X. Zheng, J. Zhu, X. Wang, Y. Yu, G. Pan, X. Xia and J. Tu, *Nano Energy*, 2019, **58**, 355-364.
58. B. Guo, X. Yu, X.-G. Sun, M. Chi, Z.-A. Qiao, J. Liu, Y.-S. Hu, X.-Q. Yang, J. B. Goodenough and S. Dai, *Energy Environ. Sci.*, 2014, **7**, 2220-2226.
59. S. Deng, H. Zhu, B. Liu, L. Yang, X. Wang, S. Shen, Y. Zhang, J. Wang, C. Ai, Y. Ren, Q. Liu, S. Lin, Y. Lu, G. Pan, J. Wu, X. Xia and J. Tu, *Adv. Funct. Mater.*, 2020, **30**, 2002665.
60. C. Jo, Y. Kim, J. Hwang, J. Shim, J. Chun and J. Lee, *Chem. Mater.*, 2014, **26**, 3508-3514.
61. K. J. Griffith, K. M. Wiaderek, G. Cibin, L. E. Marbella and C. P. Grey, *Nature*, 2018, **559**, 556-563.
62. L. Yan, H. Lan, H. Yu, S. Qian, X. Cheng, N. Long, R. Zhang, M. Shui and J. Shu, *J. Mater. Chem. A*, 2017, **5**, 8972-8980.
63. L. Yan, J. Shu, C. Li, X. Cheng, H. Zhu, H. Yu, C. Zhang, Y. Zheng, Y. Xie and Z. Guo, *Energy Storage Mater.*, 2019, **16**, 535-544.
64. X. Lou, C. Lin, Q. Luo, J. Zhao, B. Wang, J. Li, Q. Shao, X. Guo, N. Wang and Z. Guo, *ChemElectroChem*, 2017, **4**, 3171-3180.
65. X. Lou, Z. Xu, Z. Luo, C. Lin, C. Yang, H. Zhao, P. Zheng, J. Li, N. Wang, Y. Chen and H. Wu, *Electrochim. Acta*, 2017, **245**, 482-488.
66. Q. Fu, H. Cao, G. Liang, L. Luo, Y. Chen, V. Murugadoss, S. Wu, T. Ding, C. Lin and Z. Guo, *Chem. Commun.*, 2019, **56**, 619-622.
67. L. Yang, X. Zhu, X. Li, X. Zhao, K. Pei, W. You, X. Li, Y. Chen, C. Lin and R. Che, *Adv. Energy Mater.*, 2019, **9**.
68. M. W. Logan, D. Zhang, B. Tan and K. Gerasopoulos, *J. Mater. Chem. A*, 2021, **9**, 11228-11240.
69. Y. Yang, H. Zhu, F. Yang, F. Yang, D. Chen, Z. Wen, D. Wu, M. Ye, Y. Zhang, J. Zhao, Q. Liu, X. Lu, M. Gu, C. C. Li and W. He, *Nano Lett.*, 2021, **21**, 9675-9683.
70. X. Zhu, H. Cao, R. Li, Q. Fu, G. Liang, Y. Chen, L. Luo, C. Lin and X. S. Zhao, *J. Mater. Chem. A*, 2019, **7**, 25537-25547.
71. X. Lou, Q. Fu, J. Xu, X. Liu, C. Lin, J. Han, Y. Luo, Y. Chen, X. Fan and J. Li, *ACS Appl. Nano Mater*, 2017, **1**, 183-190.
72. X. Cai, H. Yan, R. Zheng, H. Yu, Z. Yang, X. Zhang, M. Xia, W. Chen, Y. Cui and J. Shu, *Inorg. Chem. Front.*, 2021, **8**, 444-451.
73. R. Zheng, S. Qian, X. Cheng, H. Yu, N. Peng, T. Liu, J. Zhang, M. Xia, H. Zhu and J. Shu, *Nano Energy*, 2019, **58**, 399-409.
74. X. Lou, R. Li, X. Zhu, L. Luo, Y. Chen, C. Lin, H. Li and X. S. Zhao, *ACS Appl. Mater. Interfaces*, 2019, **11**, 6089-6096.
75. Y. Li, R. Zheng, H. Yu, X. Cheng, T. Liu, N. Peng, J. Zhang, M. Shui and J. Shu, *ACS Appl. Mater. Interfaces*, 2019, **11**, 22429-22438.
76. C. Yang, Y. Zhang, F. Lv, C. Lin, Y. Liu, K. Wang, J. Feng, X. Wang, Y. Chen and J. Li, *J. Mater. Chem. A*, 2017, **5**, 22297-22304.
77. X. Zhu, J. Xu, Y. Luo, Q. Fu, G. Liang, L. Luo, Y. Chen, C. Lin and X. S. Zhao, *J. Mater. Chem. A*, 2019, **7**, 6522-6532.
78. Q. Fu, X. Liu, J. Hou, Y. Pu, C. Lin, L. Yang, X. Zhu, L. Hu, S. Lin, L. Luo and Y. Chen, *J. Power Sources*, 2018, **397**, 231-239.
79. Q. Fu, R. Li, X. Zhu, G. Liang, L. Luo, Y. Chen, C. Lin and X. S. Zhao, *J. Mater. Chem. A*, 2019, **7**, 19862-19871.
80. A. A. Hubaud, D. J. Schroeder, B. J. Ingram, J. S. Okasinski and J. T. Vaughey, *J. Alloys Compd.*, 2015, **644**, 804-807.
81. N. Anantharamulu, K. Koteswara Rao, G. Rambabu, B. Vijaya Kumar, V. Radha and M. Vithal, *J. Mater. Sci.*, 2011, **46**, 2821-2837.

82. E. J. Cheng, K. Hong, N. J. Taylor, H. Choe, J. Wolfenstine and J. Sakamoto, *J. Eur. Ceram. Soc.*, 2017, **37**, 3213-3217.
83. Y. Touloukian, R. Kirby, R. Taylor and T. Lee, *New York*, 1970, 89.